



**HAL**  
open science

# Paleoclimatic Tracers' An Investigation Using an Atmospheric General Circulation Model Under Ice Age Conditions

Sylvie Joussaume

► **To cite this version:**

Sylvie Joussaume. Paleoclimatic Tracers' An Investigation Using an Atmospheric General Circulation Model Under Ice Age Conditions. *Journal of Geophysical Research: Atmospheres*, 1993, 98 (D2), pp.2767-2805. 10.1029/92JD01921 . hal-03334788

**HAL Id: hal-03334788**

**<https://hal.science/hal-03334788>**

Submitted on 5 Sep 2021

**HAL** is a multi-disciplinary open access archive for the deposit and dissemination of scientific research documents, whether they are published or not. The documents may come from teaching and research institutions in France or abroad, or from public or private research centers.

L'archive ouverte pluridisciplinaire **HAL**, est destinée au dépôt et à la diffusion de documents scientifiques de niveau recherche, publiés ou non, émanant des établissements d'enseignement et de recherche français ou étrangers, des laboratoires publics ou privés.

# Paleoclimatic Tracers: An Investigation Using an Atmospheric General Circulation Model Under Ice Age Conditions

## 1. Desert Dust

SYLVIE JOUSSAUME<sup>1</sup>

*Laboratoire de Météorologie Dynamique, Centre National de la Recherche Scientifique, Paris, France*

Many studies with atmospheric general circulation models (AGCMs) have demonstrated their usefulness in reconstructing past climates. In a new approach, we have used an AGCM to investigate the link between tracer cycles and climate. We consider in this paper the atmospheric cycle of windblown dust material from desertic areas and in part 2 the water isotope cycles. Studies from ice cores have shown a strong increase of the dust deposits during glacial periods, both over East Antarctica and Greenland. We do not know, however, whether this past increase is global or just a local feature, where the dust came from, and what are the mechanisms yielding this increase. We try to answer to these questions by using an AGCM including a model for the desert dust cycle to simulate the present-day and Last Glacial Maximum climates for February and August. The model simulates only a weak increase of the global atmospheric dust content. Stronger variations are obtained at a regional scale and are in good agreement with observations from deep-sea sediments. However, the model does not reproduce the great increase of the dust concentration in snow that has been observed in ice cores. Several model deficiencies can induce this model-data discrepancy as, for example, inaccuracies of the circulation patterns or of the dust model. However, most likely, the model fails to simulate the actual sources of dust.

### 1. INTRODUCTION

The reconstruction of past climates helps to illustrate the mechanisms of climatic changes. The paleoclimatic data are diverse and include for example pollen, marine plankton, stable water isotopes and dust particles, extracted from diverse substrata, like marine sediments, lake varves and ice cores. Relatively few climatic variables can be directly measured from these data and most climatic reconstructions must be inferred indirectly through an interpretation of the data. For example, changes in the oxygen 18 and deuterium content of ice cores are interpreted in terms of changes in surface air temperature as is discussed by *Joussaume and Jouzel* [this issue] referred to as part 2 in this paper. The interpretation of some types of data, however, can be difficult when several factors make the data sensitive to climatic changes, as it is the case for dust particles.

Ice core studies in Greenland and Antarctica have displayed a strong increase in the amount of dust particles deposited during the Last Glacial Maximum (referred to as LGM or ice age in the text), dated at 18,000 years before present (B.P.) and more recently at 21,000 years B.P. by *Bard et al.* [1990]. At Camp Century in Greenland, the ice age concentration is 100 times the present value [*Thompson, 1977a*], at Dôme C and Vostok stations in East Antarctica, it is 10 to 20 times [*Petit et al., 1981; De Angelis et al., 1987*], and at Byrd Station in West Antarctica, 4 times [*Thompson, 1977a*]. Recent analyses obtained over the whole last glacial-interglacial cycle at

Vostok station in Antarctica have even shown that each cold stage is accompanied by an increase in the dust content of the ice, except for the glacial period centered around 110,000 years B.P. [*De Angelis et al., 1987*].

The interpretation of the dust-climate relationship is not straightforward. The dust contained in ice cores is from continental origin, as is deduced from its aluminium content, whereas volcanism appears negligible, except at Byrd Station. The dust increase can then result from changes in the source regions, in the dust transport or in the removal intensity. *Petit et al.* [1981] interpreted the changes observed in the Antarctic ice cores as resulting from an increased extent of the desert regions and from an intensification of the meridional transport around Antarctica. The change in desert dust extent is supported by fossil dune studies [*Sarnthein, 1978*]. The increase in the meridional transport is supported by the increased amount of sea salt particles found in ice cores during the LGM [*Petit et al., 1981; De Angelis et al., 1987*]. To investigate this problem, we propose to use an atmospheric general circulation model (AGCM) to simulate the climate of the LGM.

AGCMs can be used to reconstruct the atmospheric circulation for snapshot periods in the past, and many such investigations have been performed for the Last Glacial Maximum [*Williams et al., 1974; Gates, 1976a, b; Manabe and Hahn, 1977; Hansen et al., 1984; Rind, 1987; Kutzbach and Guetter, 1986; Manabe and Broccoli, 1985; Broccoli and Manabe, 1987; Lautenschlager and Herterich, 1989, 1990*]. These studies require us to prescribe the boundary conditions corresponding to the LGM climate conditions, i.e., the sea surface temperature (SST), the sea ice and ice sheet extents, and the vegetation cover through the albedo parameter, which have been gathered by the "Climate: Long-Range Investigation, Mapping and Prediction" (CLIMAP) group [*CLIMAP, 1976, 1981*]. As a complementary approach, we propose to use the reconstructions of past climates to investigate the relationship between climate and paleoclimatic tracers: desert dust

<sup>1</sup> Now at Laboratoire de Modélisation du Climat et de l'Environnement, Commissariat à l'Energie Atomique, Gif-sur-Yvette, and also at Laboratoire d'Océanographie Dynamique et de Climatologie, Centre National de la Recherche Scientifique, Paris, France.

particles in this paper and water isotopes in part 2.

Simulations of the ice age and present-day climates have been performed with the AGCM of the Laboratoire de Météorologie Dynamique (LMD), which includes a modeling of the desert dust and water isotope cycles. The simultaneous simulation of tracers and climatic variables for different climatic conditions should then allow us to investigate the climate-tracer relationship. This new approach should also allow a direct comparison between paleoclimatic data and simulated climates. After a brief description of the modeling of the desert dust cycle in section 2 and of the numerical experiments in section 3, we will discuss the model results for the ice age climate in sections 4 and 5 and the dust results in sections 6 and 7.

## 2. MODEL DESCRIPTION

Joussaume [1990] described the modeling of the atmospheric cycle of desert dust particles together with the simulated results for the present-day climate and the comparison with observations. We, therefore, only describe here the main aspects of the LMD AGCM and of the dust modeling.

### 2.1. The General Circulation Model

The LMD AGCM is a grid point model with 64 points regularly spaced in longitude, and 50 points regularly spaced in sine of latitude. Therefore, the model resolution is good in the tropics with a mesh size of  $625 \times 225 \text{ km}^2$  and corresponds to  $400 \times 400 \text{ km}^2$  at  $50^\circ$  of latitude. The model has 11 layers in normalized pressure coordinate ( $\sigma$ ), with four layers in the planetary boundary layer, four in the free troposphere and three in the stratosphere. The model is based on the dynamic, mass continuity, water vapor conservation and thermodynamic equations. It includes parameterizations of condensation and diffusion processes and a one-layer model for the soil water and temperature reservoir [Sadourny and Laval, 1984]. The predicted clouds are considered for the radiative transfers [Le Treut and Laval, 1984].

The version used in the present paper slightly differs from the previous ones with regard to the horizontal diffusion scheme used for the enthalpy, and the divergence and curl of the wind. The bilaplacian operator used acts along pressure surfaces rather than  $\sigma$  surfaces, in order to avoid the forced diffusion resulting from the curvature of the  $\sigma$  isolines above orography. This scheme improves the simulated planetary wave pattern of the northern hemisphere winter circulation, in particular above the Rocky Mountains [Michaud, 1987; Michaud, 1990]. The vertical transport of water vapor is also modified when including the tracers: arithmetic means are replaced by harmonic means between adjacent grid points, in order to avoid negative mixing ratios which are critical for the transport of water isotope species [Joussaume et al., 1984].

### 2.2. Desert Dust Modeling

In this first approach of a desert dust modeling within an AGCM, many oversimplified parameterizations have been used. Only one size range of particles has been introduced, around  $1 \mu\text{m}$ , in order to represent the particles which experience long-range transport. Moreover, the particles are considered as passive scalars with no interaction with radiation or condensation processes.

A prognostic equation for the dust mass has been included, which takes into account the dust sources, the vertical turbulent diffusion occurring within the planetary boundary layer, the large-scale transport by simulated winds, the vertical convective diffusion associated with convective dry and wet adjustment processes, and the removal of dust. Specific to dust modeling are the source and removal terms.

*Source.* Dust particles are raised by the simulated surface winds over desertic areas. The mobilization flux intensity  $s_p$  is parameterized using a bulk aerodynamic formula similar to the one commonly used for water vapor:

$$s_p = (\Delta z_1)^{-1} \rho_a C_{Dp} (1 + |\mathbf{V}_1|) \beta_p (q_{ps} - q_{pa}) \quad (1)$$

with  $\Delta z_1$ , the first layer thickness in  $z$  coordinate;  $\rho_a$ , the surface air density;  $\mathbf{V}_1$ , the wind velocity at the first  $\sigma$  level of the model and  $1 \text{ m s}^{-1}$  a minimum wind velocity ensuring a minimum turbulent flux;  $\beta_p$ , a control parameter equal to 1 over source areas and zero elsewhere; and  $q_{pa}$ , the dust particle mixing ratio (mass of dust over mass of air) near the surface. For the drag coefficient  $C_{Dp}$ , the same values have been used for dust and water vapor, i.e., set to a constant value differing over land and oceans and for the winter and summer seasons in order to account for the higher turbulence occurring during the winter season and over land. The flux formulation also depends on a saturation dust mixing ratio at the surface,  $q_{ps}$ , which has been assumed to be constant and then set arbitrarily equal to 1 since all the dust parameterizations are linear. Dust units are therefore defined except for an arbitrary constant. In the following, the dust mass units will be referred to as kgAU (Kilograms arbitrary units). However, our dust parameterization defined that way is highly simplified. Indeed, observations show that mobilization only occurs for strong enough surface wind velocities [Gillette et al., 1980]. Moreover, we have assumed a linear dependence of  $s_p$  with the surface wind speed, whereas observations show a dependence in the third or fourth power of the surface wind speed [Gillette, 1979]. This shortcoming of our modeling results from a programming error where  $q_{ps}$  has been set as constant rather than proportional to the second or third power of the surface wind speed.

The extents of the source areas are parameterized and not prescribed in order to generate the source areas during the ice age simulations directly from the model results. The source areas are defined as the regions where the soil water content, averaged over the winter and summer seasons, is less than  $2 \text{ mm d}^{-1}$ , i.e., less than 1.3% of the maximum soil water capacity. The source regions are therefore taken to be identical for both seasons. This criterion has been chosen in order to reproduce reasonably well the extent of the simulated desert areas for the present-day climate compared to observations [Joussaume, 1990]. However, with this criterion, the model underestimates the Australian source.

*Removal.* The wet removal of particles occurs when particles act as condensation nuclei or are scavenged by falling drops. The latter process however can be neglected for small enough particles (in the  $1\text{-}\mu\text{m}$  range) [Slinn, 1983]. The main process involved then is the formation of condensed water around condensation nuclei. The amount of particles removed by the condensed water is usually set proportional to the local amount of particles [Slinn, 1983] with, however, a large uncertainty in the value of the proportionality coefficient. In our first approach, we assume that dust and water vapor are

removed from the cloud layer with the same efficiency, or, in other words, that their respective lifetimes are the same for this process [Joussaume, 1990].

A gravitational settling velocity has also been included, although very weak in the 1- $\mu\text{m}$  size range (30  $\text{m d}^{-1}$ ). More important is the deposition of dust at the surface resulting from turbulence and interception by obstacles. We use the bulk aerodynamic formula (1) to account for turbulence and we assume that the surface is a perfect sink by setting  $q_{ps} = 0$ .

For the present-day climate, the simulated results for the dry and wet removal efficiencies have been compared to the few available observations given by Joussaume [1990]. The main conclusions of this study are that the dry removal flux prevails over the wet one in the model, except for regions far from the source areas, and that the efficiency of the surface dry removal process seems to be overestimated in the model, whereas the wet removal efficiency is too small.

*General comments.* The overall patterns of the dust transport appear reasonable, at least qualitatively, when compared to the available observations [Joussaume, 1990]. For example, the model reproduces the long-range transport of Saharan dust over the northern tropical Atlantic Ocean in August and the transport of Asian dust over the Pacific in February. However, some simulated features disagree, such as an overestimated eastward transport of Saharan and Arabian-Asian dust in August as well as an overestimation of the August Australian dust plumes. Most of these discrepancies result from discrepancies in the simulated wind fields themselves. They can also be due to failures of the desert dust modeling, which are, however, difficult to emphasize because of our rather poor knowledge of the global distributions of the dust atmospheric content, sources and sinks. Therefore, the simulated results concerning the dust-climate relationship must certainly be considered very cautiously and only as a first attempt to investigate the dust-climate relationship.

### 3. NUMERICAL EXPERIMENTS

#### 3.1. Boundary Conditions

The LMD AGCM has been run under ice age and present-day climatic conditions, the latter being considered as the control runs. The glacial boundary conditions, sea surface temperature, sea ice, ice sheets and surface albedo have been prescribed according to the CLIMAP [1981] data set (Figure 1). The continental outlines have been modified to account for the sea level reduction of 150 m which corresponds to the accumulation of ice over the continents during the LGM. To be consistent with the CLIMAP data set, the model has been run under perpetual August and perpetual February conditions using the midmonth incoming solar radiation. The glacial orbital parameters have been computed according to Berger [1978]. Only the seasonal Earth-Sun distance is affected, leading to weak changes in the mean incoming solar radiation, i.e., 1.2% in August and +1.2% in February. The atmospheric  $\text{CO}_2$  concentration has been lowered from 330 ppm to 190 ppm for the LGM to account for the results obtained from ice core studies [Barnola et al., 1987].

#### 3.2. Surface Albedo

The CLIMAP [1981] data set also provides boundary conditions for the present-day climate which have been used in

the control runs. Using the CLIMAP data set for both climatic conditions allows for a better consistency between modern and ice age simulations especially for the albedo field. Indeed, differences between two albedo data sets for present-day conditions may exceed the differences between present-day and ice age conditions given by CLIMAP; e.g., over the Sahara, the CLIMAP albedo lies around 35% for both climatic conditions and is much stronger than the value of 25% used in the previous experiments performed with the LMD model [Bartman, 1980]. Moreover, CLIMAP [1981] gives albedo values for dry ( $A_d$ ) and wet ( $A_w$ ) soil conditions as well as for snow cover ( $A_s$ ). We have thus introduced in the model a parameterization of the surface albedo  $A$  which is interactive with the soil water content  $w$  and the snow cover  $s$ :

$$A = \min \left( \left( 1 - \frac{s}{s_0} \right) A' + \frac{s}{s_0} A_s, A_s \right) \quad \text{with} \quad (2)$$

$$A' = \frac{w}{w_{max}} A_w + \left( 1 - \frac{w}{w_{max}} \right) A_d$$

where  $s_0$  is the minimum 25-cm snow depth at which the snow albedo value can be used, and  $w_{max}$  is the maximum soil water reservoir of the model (150 mm). Nevertheless, the time variability of  $A$  resulting from (2) is weak and has certainly only a minor impact on the model results.

CLIMAP [1981] also gives albedo values for an incident solar angle less than  $60^\circ$ . To compute the midmonth daily mean albedo used in the model, the albedo has been multiplied by a function of the zenith solar angle  $\theta$  to account for increasing albedo values with increasing  $\theta$  values. The functions used differ over land, ocean and snow-ice surfaces and are based on the work of Larson and Barkstrom [1977].

The averaged global surface albedo increases during the LGM by 0.06 (Table 1), first by an increase in snow and ice areas and second by a decrease in forest areas, e.g., over Europe or the Amazon Basin (Figure 2).

#### 3.3. Initial Conditions

Starting from the atmospheric meteorological conditions of January 21 and June 11, 1979, simulations have been run over 160 and 200 days for present-day and ice age conditions respectively. For ice age experiments, the hydrostatic equilibrium was restored in the modern initial surface pressure field to account for the elevated ice sheets. However, the atmospheric mass was not reset to its modern value, leading to a mean annual shift of -13.5 hPa in the global surface pressure field (Table 1). The groundwater reservoir was initialized from previous simulations of the LMD AGCM of January and July conditions.

The tracers, desert dust particles and water isotopes, have only been introduced in the modern and ice age simulations after 60 and 100 days, respectively, in order to avoid the spin-up time of the model requested to reach an atmospheric circulation consistent with the prescribed boundary conditions. The dust model starts with no dust atmospheric content.

The initial extent of the source areas is defined using the soil water content parameter which has been averaged over the last 40 days preceding the introduction of tracers and has been averaged over the February and August simulations. However, soil moisture is a slow evolving variable and we may not have converged yet toward the model generated dry regions. The simulated source regions are therefore updated every 10 days of

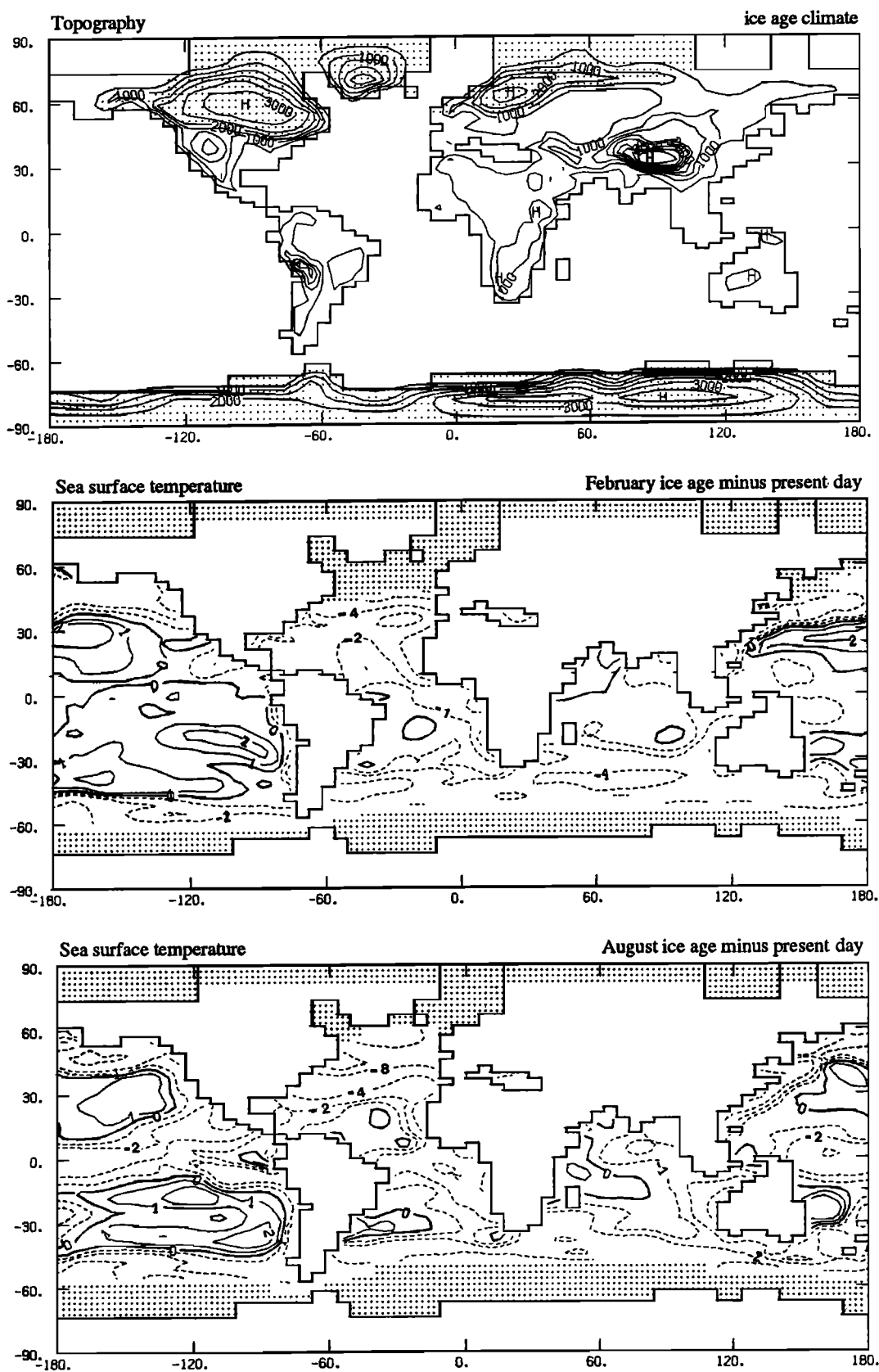


Fig. 1. Boundary conditions for the ice age simulations: topography (top), sea ice extent (dotted areas) and the ice age minus present-day change in sea surface temperature (SST) for February (middle) and August (bottom). Isolines: for the topography at every 500 m and for the SST field at every 1°C above -2°C and at every 4°C below -4°C.

TABLE 1. Global Budgets of the Simulated Atmospheric Circulation of the February and August Present Day and Ice Age Climates

	Northern Hemisphere		Southern Hemisphere		Global		Ice Age Minus Present
	Present	Ice Age	Present	Ice Age	Present	Ice Age	
<i>February</i>							
Surface air temperature, °C	9.4	4.7	15.5	14.0	12.4	9.3	-3.1
Vertically integrated air temperature, °C	-31.4	-33.0	-27.7	-28.3	-29.6	-30.6	-1.0
Surface pressure, hPa	985.6	964.0	991.7	985.5	988.6	974.8	-13.8
Mean kinetic energy, m <sup>2</sup> s <sup>-2</sup>	179.0	219.0	96.8	114.5	137.8	166.2	+21%
Precipitable water, cm	2.24	1.93	3.07	2.92	2.65	2.42	-9%
Precipitation, mm d <sup>-1</sup>	2.71	2.45	3.33	3.58	3.02	3.01	-0.3%
Evaporation, mm d <sup>-1</sup>	3.02	2.87	3.02	3.17	3.02	3.02	0%
Soil moisture, mm	102.3	89.1	126.5	118.4	114.4	103.7	-9%
Incident solar radiation, W m <sup>-2</sup>	268.6	272.1	424.4	429.9	346.5	351.0	+4.5
Planetary albedo, %	32.3	33.4	32.0	34.5	32.2	34.1	+1.9
Surface albedo, %	24.6	31.7	13.7	19.7	19.1	25.7	+6.6
Net radiation at the top, W m <sup>-2</sup>	-37.1	-36.9	58.1	50.6	10.5	6.9	-3.7
Surface heat balance, W m <sup>-2</sup>	34.7	33.7	-53.2	-41.3	-9.3	-3.7	+5.6
Net heating rate, W m <sup>-2</sup>	-11.2	-15.2	13.7	21.0	1.2	3.2	+2.0
<i>August</i>							
Surface air temperature, °C	21.7	16.9	10.9	7.6	16.3	12.2	-4.1
Vertically integrated air temperature, °C	-23.1	-26.5	-30.3	-31.9	-26.7	-29.3	-2.6
Surface pressure, hPa	984.0	962.5	993.7	988.6	988.9	975.6	-13.3
Mean kinetic energy, m <sup>2</sup> s <sup>-2</sup>	72.4	104.0	206.7	196.4	139.9	150.8	+8%
Precipitable water, cm	3.63	2.86	2.27	2.03	2.95	2.45	-17%
Precipitation, mm d <sup>-1</sup>	3.90	3.66	2.37	2.42	3.14	3.04	-3%
Evaporation, mm d <sup>-1</sup>	3.16	2.98	3.07	3.09	3.12	3.04	-3%
Soil moisture, mm	101.0	94.8	115.7	107.2	108.4	101.0	-7%
Incident solar radiation, W m <sup>-2</sup>	406.8	402.0	252.9	249.8	330.0	326.0	-4.0
Planetary albedo, %	29.6	33.4	29.4	30.5	29.5	32.3	+2.8
Surface albedo, %	13.9	22.1	20.8	25.3	17.3	23.7	+6.4
Net radiation at the top, W m <sup>-2</sup>	39.8	27.4	-46.4	-50.7	-3.3	-11.6	-8.3
Surface heat balance, W m <sup>-2</sup>	-25.9	-16.2	38.0	42.1	6.1	14.0	+7.9
Net heating rate, W m <sup>-2</sup>	34.6	30.1	-28.4	-25.8	2.8	2.4	-0.4

simulation by increasing the soil moisture time average used to predict them. The source areas can then vary slightly along the simulation, although the convergence is practically achieved at the beginning of the dust simulation.

In the following, the model results are averaged over the last 60 days of each simulation, since 40 days are required to reach an equilibrium of the global atmospheric content of tracers. A 60-day time average is too small to account for the low frequency of the atmospheric circulation. However, the computing time was restricted by the high requirements of the tracer models. The internal atmospheric variability may thus bias some of the simulated atmospheric circulation patterns and consequently some features of the dust cycle. To better emphasize the model sensitivity to the ice age boundary conditions, we infer the model variability from two sets of three numerical experiments performed for February and August present-day conditions [Michaud, 1987; Braine-Bonnaire, 1989]. Nevertheless, our present tracer experiments must be considered as a first approach, more of meteorological than of climatological relevance, that can help diagnose some of the main aspects of the dust-climate relationship but that cannot bring an extensive study of the problem.

#### 4. MODEL-DATA COMPARISONS FOR THE ICE AGE CLIMATE

If we want to investigate the link between tracers and climate using AGCM simulations of past climates, we must first test the reliability of the simulated climate. For the present-day conditions, the simulated climate was discussed by Joussaume [1990]. For the LGM, we compare the model results to climatic estimates from paleoclimatic data. Besides the test of the model abilities, the simulations also offer the opportunity to reconstruct the ice age atmospheric circulation, as will be discussed in section 5.

For the comparison with climatic estimates from past data, we estimated annual means from the model results by averaging the August and February means since no seasonal cycle was included. Some further comparisons on a seasonal basis will be conducted when considering some specific aspects of the reconstructed circulation of the LGM climate (section 5). We focus here on the surface air temperature and on the precipitation which are the two climatic variables most easily estimated from past data. We also use the precipitation minus evaporation field which is more relevant than

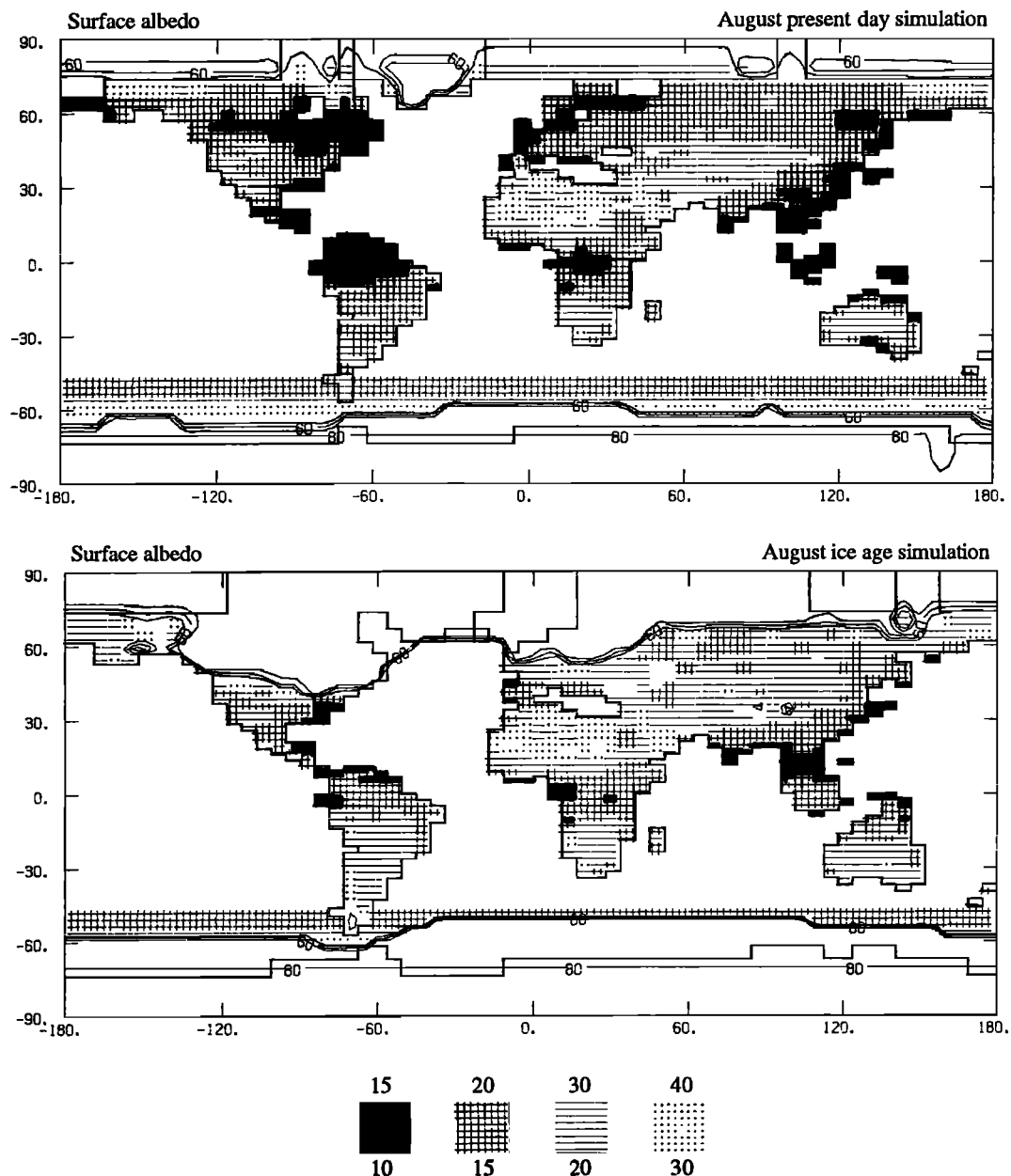


Fig. 2. Surface albedo (percent) for the August present day and ice age simulations. Shaded areas between 10% and 40% and isolines at every 10% above 50%.

precipitation when compared to water levels in lakes. We mainly refer to the compilation of past data for the LGM given by *Peterson et al.* [1979], updated whenever possible by more recent works [*Street-Perrot and Harrison, 1985*].

#### 4.1. Surface Air Temperature

The simulated global cooling is 3.1°C in February and 4.1°C in August leading to an annual mean change of 3.6°C (Table 1). This value is similar to the results obtained by other AGCM simulations based on the same boundary conditions [*Kutzbach and Guetter, 1986; Rind, 1987; Lautenschlager and Herterich, 1989*] (Table 2). The cooling is not uniform: it is smaller in tropical regions (1.2°C) and increases with latitude, with a cooling of 10.7°C and 5.4°C above 60° in the northern and southern hemisphere, respectively. The cooling is particularly large over ice sheets and sea ice in the northern

hemisphere and over sea ice in the southern hemisphere (Figure 3). It induces stronger meridional temperature gradients around 40°N-60°N and 60°S.

The simulated change in surface air temperature (Figure 3) can be compared to paleoclimatic data over the continents only, since past data over the oceans were already used as a fixed boundary condition for the model.

In the northern hemisphere, the simulated surface air temperature is 15°C lower than today at the southern edge of the Laurentide and Fennoscandian ice sheets and only 2°C lower than today farther south of the ice sheets. Over North America, the simulated cooling is less on the west coast than on the east coast. The small cooling of 2° to 4°C simulated over the southwestern coast is well corroborated by paleoclimatic data, as well as the stronger cooling trend northward and eastward with values reaching 5°C to 8°C [*Peterson et al., 1979*]. Over eastern North America, the

TABLE 2. Comparison of Global Budgets for Present Day and Ice Age Simulations Obtained by Various AGCMs

AGCMs	NH WINTER		NH SUMMER	
	Present	Ice Age Minus Present	Present	Ice Age Minus Present
<i>Surface air temperature (°C)</i>				
Oregon State University (OSU)			17.5	-4.9
Geophysical Fluid Dynamics Laboratory (GFDL)				-5.4
National Center for Atmospheric Research (NCAR)	10.6	-3.7	15.8	-3.9
Goddard Institute for Space Studies (GISS)	11.8	-3.3	15.0	-3.4
Max Planck Institut für Meteorologie (MPIM)	12.1	-4.2	15.7	-5.4
Laboratoire de Météorologie Dynamique (LMD)	12.4	-3.0	16.3	-4.1
<i>Precipitation (mm d<sup>-1</sup>)</i>				
Oregon State University (OSU)			4.5	-14%
Geophysical Fluid Dynamics Laboratory (GFDL)			2.9	-10%
National Center for Atmospheric Research (NCAR)	3.6	-3%	3.9	-7%
Goddard Institute for Space Studies (GISS)	3.1	<-1%	3.3	-7%
Max Planck Institut für Meteorologie (MPIM)	2.3	<-1%	2.3	-3%
Laboratoire de Météorologie Dynamique (LMD)	3.0	<-1%	3.1	-3%

References are as follows: OSU, *Gates [1976b]*; GFDL, *Manabe and Hahn [1977]*; NCAR, *Kutzbach and Guetter [1986]*; GISS, *Rind [1987]*; MPIM, *Lautenschlager and Herterich [1989]*; and LMD, this paper. The OSU and GFDL simulations use the *CLIMAP [1976]* data set while the others use the *CLIMAP [1981]* data set.

cooling is reasonable, between 3° and 5°C, except on the southern coast [*Webb et al., 1987*] where the model is certainly highly sensitive to the relatively warm waters of the Gulf of Mexico. Over western Europe, the simulated cooling goes from 5° to 8°C in the south to 15°C near the ice sheet.

These values are reasonable compared to those of *Peterson et al. [1979]* and to the 10°-12°C cooling estimated from the Grande Pile/Les Echets pollen sequences in the Vosges (France) by *Guiot [1990]*. The simulated cooling decreases toward the east with values of 3° to 6°C in southeastern Europe and in the Middle East. However, this latter trend is not corroborated by paleoclimatic data which indicate cooling of around 10° to 12°C [*Peterson et al., 1979*]. The origin of this discrepancy will be discussed when considering the atmospheric circulation in section 5.

For the higher latitudes, few estimates are available. In Alaska, a temperature decrease of 6° to 8°C is estimated from pollen data [*Peterson et al., 1979*] and is fairly well reproduced by the model in the southernmost areas but not to the north where the decrease lies between 0° and 2°C (Figure 3). Over the present-day ice sheets, estimates can be obtained from the water isotopic contents of the deep ice cores (part 2). In Greenland, *Dansgaard and Oeschger [1989]* estimate a decrease of 10° to 16°C from southern to northern cores, in good agreement with the 11° to 14°C simulated decrease. In East Antarctica, the simulated decrease of temperature is about 8°C and is well corroborated by the temperature estimates of 6° to 7°C deduced from ice cores in Vostok and Dôme C [*Lorius et al., 1979; Jouzel et al., 1987*]. However, this agreement is weakened when considering the changes in surface elevation, since the model prescribes a 500-m increase in the surface elevation following the *CLIMAP [1981]* estimate, whereas ice core studies from Antarctica tend to indicate a lowering of several hundred meters (*D. Raynaud, private communication, 1989*).

In tropical continental regions, the simulated decrease is less than 3°C, except for Africa where it can reach 5°C in the vicinity of Arabia. Such a cooling, although stronger than over the oceans, is much less than the 5° to 8°C temperature decrease estimated from pollen and geomorphological data, particularly in South America, Indonesia and New Guinea [*Peterson et al., 1979*]. This discrepancy is not unique to our simulations but is common to all the simulations based on the *CLIMAP [1981]* SSTs [*Kutzbach and Guetter, 1986; Rind, 1987*]. This problem was emphasized by *Rind and Peteet [1985]*, who assessed that it could partly result from the

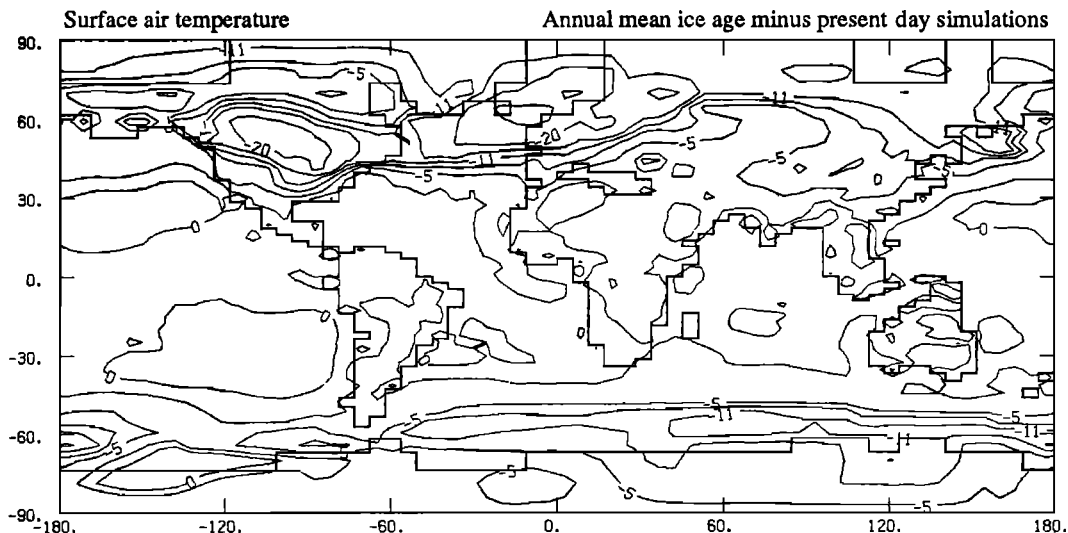


Fig. 3. Surface air temperature: simulated annual mean ice age minus present day change. Isolines at 0°C, at every 3°C between -2°C and -14°C, and at every 6°C below -14°C.

relatively warm SSTs given by *CLIMAP* [1981] for most tropical oceanic areas. Indeed, stronger continental temperature coolings were simulated in numerical experiments based on colder SSTs, i.e., in experiments by *Rind and Peteet* [1985] or in the experiments based on the previous *CLIMAP* [1976] data set by *Gates* [1976a, b] and *Manabe and Hahn* [1977]. But other reasons can also generate this model-data discrepancy. Model deficiencies can certainly be involved. The interpretation of past data may also be questioned. Indeed, in equatorial eastern Africa the use of modern analogues to interpret pollen data has weakened the first temperature depression estimate from 5°-8°C [*Bonnefille and Riollet*, 1988] to 4°C ±2°C [*Bonnefille et al.*, 1990]. The new estimate improves the model-data comparison and is in particularly good agreement with the values obtained with the LMD model in this area (between 2° and 4°C). Nevertheless, the comparisons of data and model results for tropical continental regions remain a critical problem.

#### 4.2. The Hydrologic Cycle

The simulated mean global hydrologic cycle is only slightly modified, with a decrease of 3% of the global mean precipitation and evaporation fluxes in August and no changes in February (Table 1). Similar trends are obtained by the other AGCM simulations, but the LMD and Max Planck Institute für Meteorologie (MPIM) AGCMs exhibit the weakest changes (Table 2). The small changes in global average correspond, however, to an increased aridity over the continents largely compensated by increased precipitation rates over oceans (Figure 4).

Over the continents, the model results can be compared to the estimates obtained from lake levels or pollen studies. Pollen data are usually interpreted in terms of changes in annual precipitation using transfer functions or other statistical methods, whereas lake levels directly reflect changes in their hydrological budget, i.e., precipitation minus evaporation changes.

The model simulates lower precipitation rates in the high latitudes, i.e., over Alaska, the northern North Atlantic, and Antarctica. These features are well corroborated by pollen and lake level studies in Alaska [*Peterson et al.*, 1979] as well as by the estimates of past snow accumulation in ice cores. The agreement is good in East Antarctica where the model simulates a decrease by a factor of 2 (Table 4 and Figure 4) corroborated by the Dôme C [*Lorius et al.*, 1984] and Vostok estimates [*Lorius et al.*, 1985]. In southern Greenland, the model overestimates the reduced snow accumulation and simulates a reduction by a factor of 10 (Table 5, Figure 4) to be compared to an estimated reduction by a factor of 2 [*Beer et al.*, 1984].

The simulated precipitation rates increase in the middle latitudes of the northern hemisphere. This trend is well corroborated by paleoclimatic data from western North America, although the model overestimates its northward extent [*Peterson et al.*, 1979]. An area of increased aridity is simulated in southeastern North America, in agreement with the pollen data there [*Peterson et al.*, 1979; *Webb et al.*, 1987]. Over Europe, south of the Fennoscandian ice sheet, the model produces a strong penetration of precipitation eastward during the ice age, whereas the aridity is increased over the Mediterranean regions. Pollen data indicate steppe vegetation during the glacial maximum over all of western Europe and in

the Middle East, which have been interpreted as being under much drier conditions [*Peterson et al.*, 1979]. According to these results, the simulated trend in southeastern Europe and in the Middle East is confirmed but not the wetter conditions over Europe. For example, *Guiot* [1990] estimates a decrease in annual precipitation of 1.5 mm d<sup>-1</sup> in eastern France, completely opposite to the simulated results. However, lakes show higher water levels during the glacial maximum in southern Europe, the Middle East and northern Africa [*Street-Perrot and Harrison*, 1985; S. P. Harrison et al., European lakes as palaeohydrological and palaeoclimatic indicators, submitted to *Quat. Sci. Rev.*, 1992] and indicate wetter conditions. These results contradict pollen data in the same areas. The origin of the discrepancy between pollen and lake levels is not clear and might result from the seasonality of the water cycle and/or from the impact of the evaporation rates on the lake levels. From the model results (Figure 4), the values for precipitation and precipitation minus evaporation exhibit similar trends over the Mediterranean region and do not allow a reconciliation of the two kinds of paleoclimatic data. It is therefore difficult to test the model results in this region before better estimates of the climatic changes are obtained from the data.

Simulated precipitation rates also decrease over most tropical continental areas, especially over the Sahara and in the Amazon Basin, in agreement with the past data [*Peterson et al.*, 1979]. However, the decreased precipitation is in large part compensated by decreased evaporation fluxes, thus leading to a small net increase in the desert extent (Figure 4 and section 6), unlike the increase inferred from fossil dune results of *Sarnthein* [1978]. The full glacial continental tropical aridity thus tends to be underestimated in our simulation. Similar results are obtained by other simulations based on the *CLIMAP* [1981] boundary conditions [*Kutzbach and Guetter*, 1986; *Rind*, 1987]. In particular, all three models simulated increased precipitation in equatorial eastern Africa, where pollen data indicate a 30% lowering of precipitation [*Bonnefille et al.*, 1990]. Stronger aridity was simulated in the previous simulations using the *CLIMAP* [1976] data set, as is emphasized by the global averages (Table 2). These features outline the large sensitivity of the model results to the prescribed SST field.

## 5. THE SIMULATED ICE AGE CIRCULATION

Simulations of past climates also provide the unique opportunity to reconstruct a comprehensive view of the atmospheric circulation whereas paleoclimatic data, which are sparsely distributed in space, can only give a partial view of it. However, such reconstructions can be model dependent, as will be illustrated. In the present paper, only few simulated fields are presented, but a more complete set of model results is discussed by *Joussaume* [1989].

### 5.1. The Tropical Atmospheric Circulation

The overall patterns of the sea level pressure in tropical areas, i.e., the low-pressure belt associated with the Inter-tropical Convergence Zone (ITCZ) and the subtropical highs over the main desertic areas, remain generally unchanged during the ice age (Figures 5 and 6).

In February, the most important change occurs over the eastern Mediterranean Sea and corresponds to the development

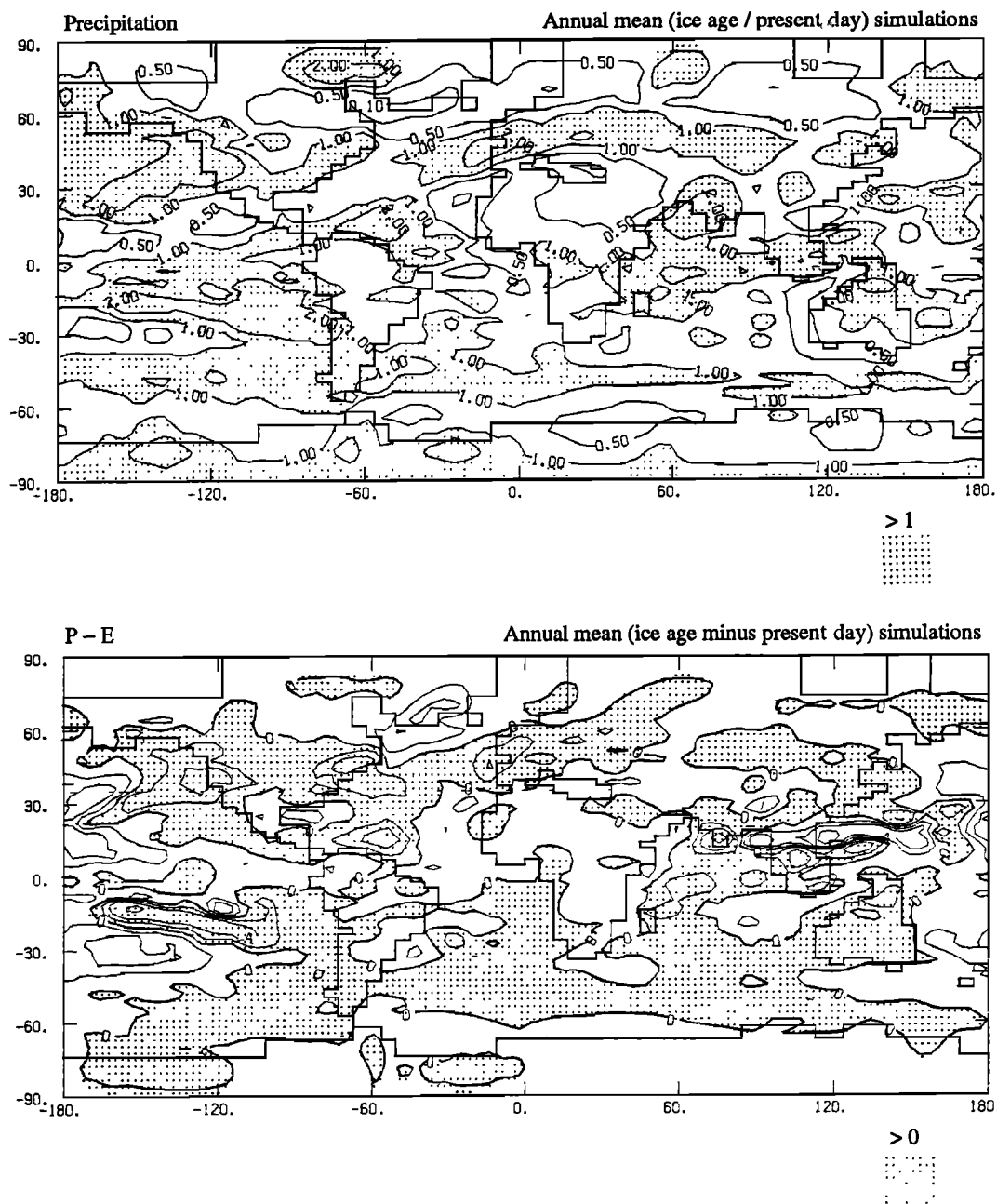


Fig. 4. (Top) Precipitation and (bottom) precipitation-minus-evaporation annual mean changes. For precipitation, the ice age/present day simulated ratio is displayed with isolines at 0.1, 0.5, 1. and 2. and dotted areas for values above 1. For the precipitation minus evaporation field, the ice age minus present-day values are displayed in millimeters per day with isolines at 0,  $\pm 2$ ,  $\pm 4$  and  $\pm 8$  and dotted areas for positive changes. Both fields are smoothed using a five-element filter (with weights of one half for the grid point and one eighth for its four nearest neighbors).

of a strong subtropical high. The associated southwesterlies on its western side induce a temperature increase over southeastern Europe (Figure 7). The Harmattan winds, i.e., the low-level northeasterly winds over North Africa, are also strengthened. These circulation features seem to result from the strong cooling of the Mediterranean surface and the related decrease of the surface latent and sensible heat fluxes. However, this circulation produces on an annual basis the weak cooling simulated over this area which is not corroborated by paleoclimatic data (section 4.1). Therefore, the strong subtropical high developing over the Mediterranean Sea seems to be invalidated.

In August, the summer monsoon circulation in India is weakened. The thermal Asian Low located over the Himalayan Plateau is reduced and the low-level southwesterlies are weakened (Figure 6). This latter change particularly affects the winds over the Gulf of Bengal and over Indonesia where the wind speed is reduced by  $5 \text{ m s}^{-1}$ , which is approximately a third of the present-day value [Joussaume, 1990]. The weakening of the thermal Asian Low is related to the strong cooling of the Himalayan Plateau (Figure 7), which is reinforced by the presence of snow through the snow albedo-temperature feedback (Figure 2). A sensitivity experiment to the only albedo change was performed by *Manabe and Hahn*

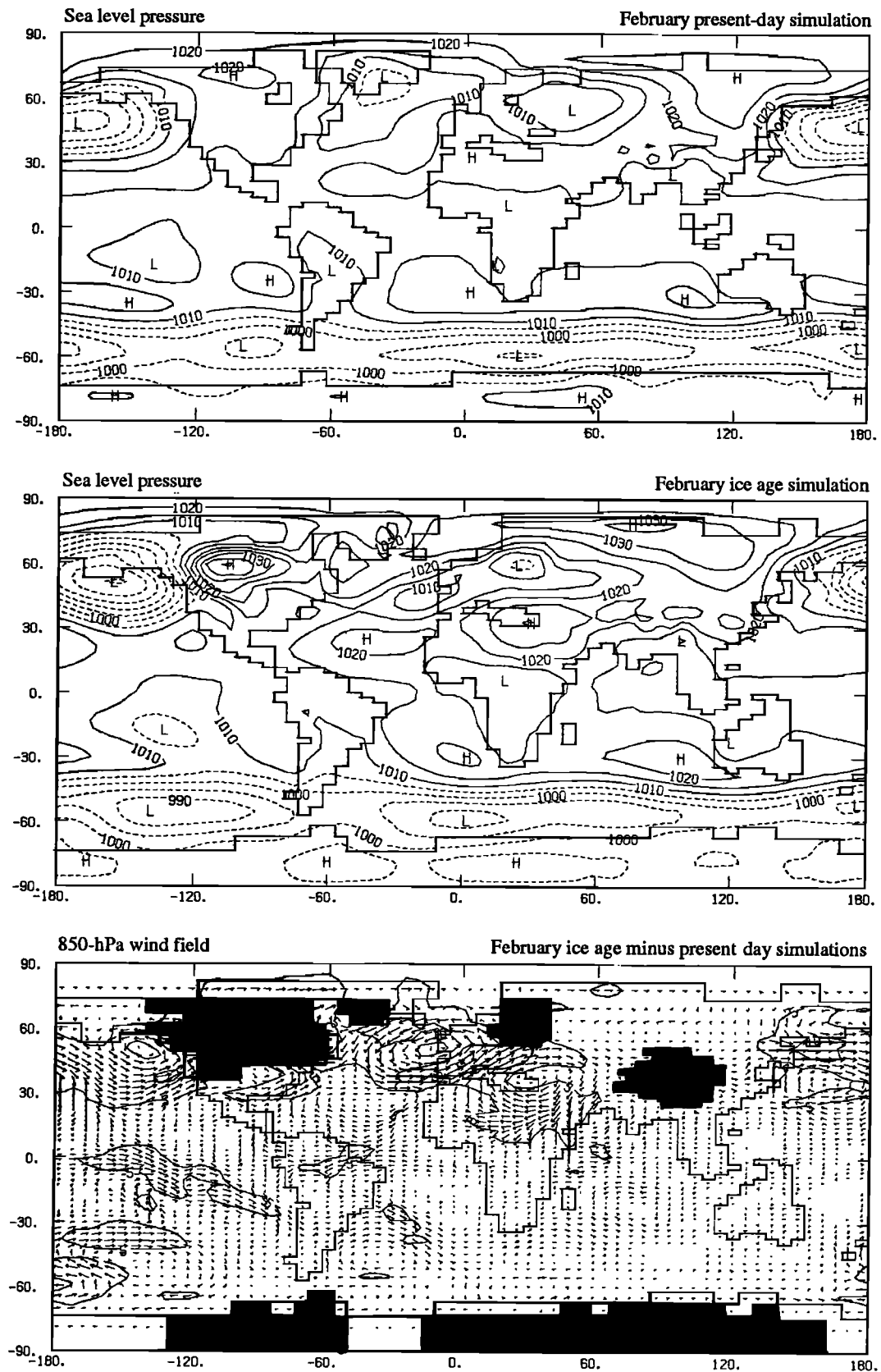


Fig. 5. Sea level pressure (hectopascals) for the (top) February present-day and (middle) ice age simulations and (bottom) February ice age minus present-day simulated change in the wind field at 850 hPa. Isolines: for the sea level pressure at every 5 hPa and dotted below 1010 hPa, for the wind intensity at every  $5 \text{ m s}^{-1}$ . Solid areas correspond to surface pressures lower than 850 hPa for the ice age simulation.

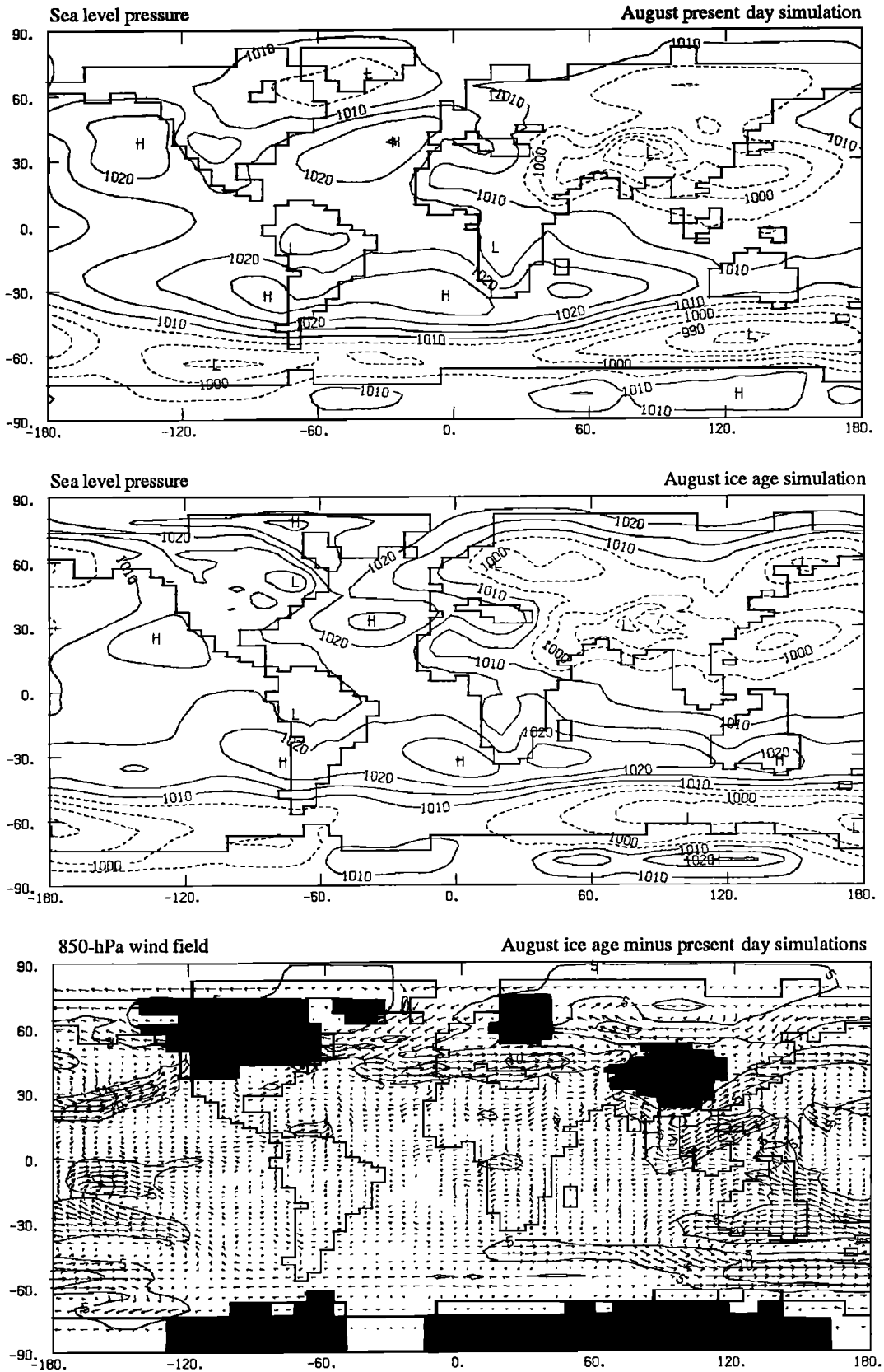


Fig. 6. Same as Figure 5 but for August.

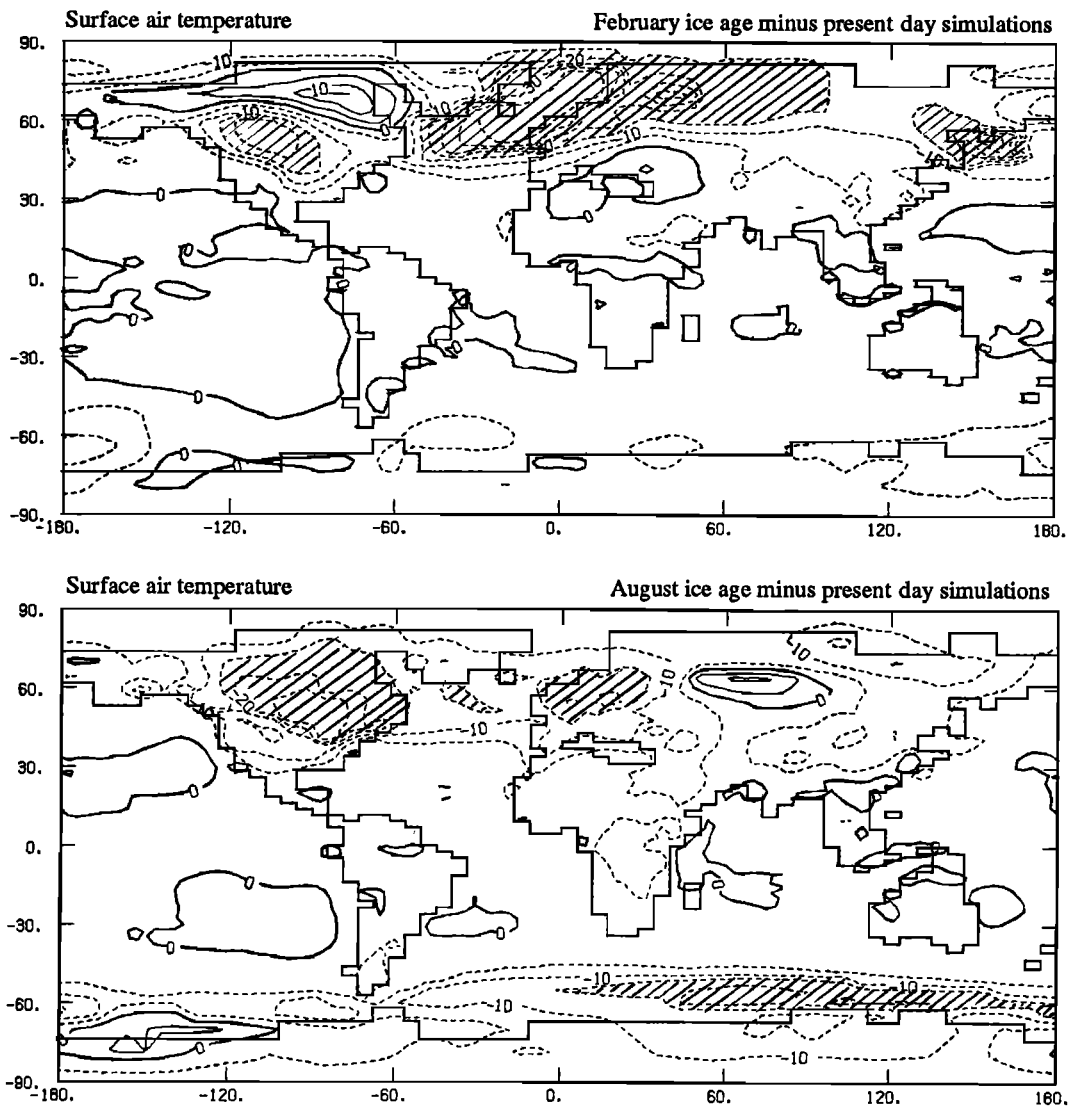


Fig. 7. Ice age minus present day changes in surface air temperature (degrees Celsius) for the (top) February and (bottom) August simulations. Isolines are at every 5°C, dotted lines are drawn below 0°C and hatched areas below -15°C.

[1977] and indeed confirmed the strong influence of the surface albedo on the monsoon intensity. The sensitivity experiments performed by Rind [1987] have also outlined the impact of the northern hemisphere ice sheets on the weakening of the Asian summer monsoon.

Monsoon rains decrease over the Gulf of Bengal, the Tibetan Plateau and Indonesia (Figure 9). In zonal average, the precipitation maximum located around 15°N, which is mainly determined by the Asian monsoon rains, is decreased by approximately 20% during the LGM. This decrease is significant, since it is persistent during all of the simulation, conversely to the simulated increase in precipitation over India. The decrease of monsoon rains is well supported by past data deduced from both pollen and salinity budgets in marine sediments of the Gulf of Bengal [Duplessy, 1982; Van Campo *et al.*, 1982]. This feature was also obtained by the other models, based on either set of CLIMAP SSTs.

Other changes are also simulated during the LGM in tropical regions. The trade winds over the tropical northern Atlantic are strengthened in association with a stronger Açores High during both the winter and summer seasons (Figures 5 and 6).

However, these changes are weak and not clearly stronger than the model variability. They may be related to transient features of the atmospheric circulation and are thus difficult to assert. In the eastern tropical south Pacific, increased precipitation is simulated during the LGM in association with low pressures (Figures 5, 6, 8, and 9). These changes are consistent with the relatively warm surface waters given by CLIMAP [1981] in this area and induce an El Niño-like climate. However, for the present-day climate, the LMD AGCM produces an excessive South Pacific Convergence Zone (SPCZ) which is displaced eastward [Joussaume, 1990]. This feature may then bias the model response to the SST change in the Pacific during the LGM.

### 5.2. Northern Hemisphere Extratropical Circulation

The most important changes in the atmospheric circulation occur in the northern hemisphere (NH) extratropical latitudes, as is expected from the important local changes in the boundary conditions.

*The low-level circulation.* The cooling is much stronger at

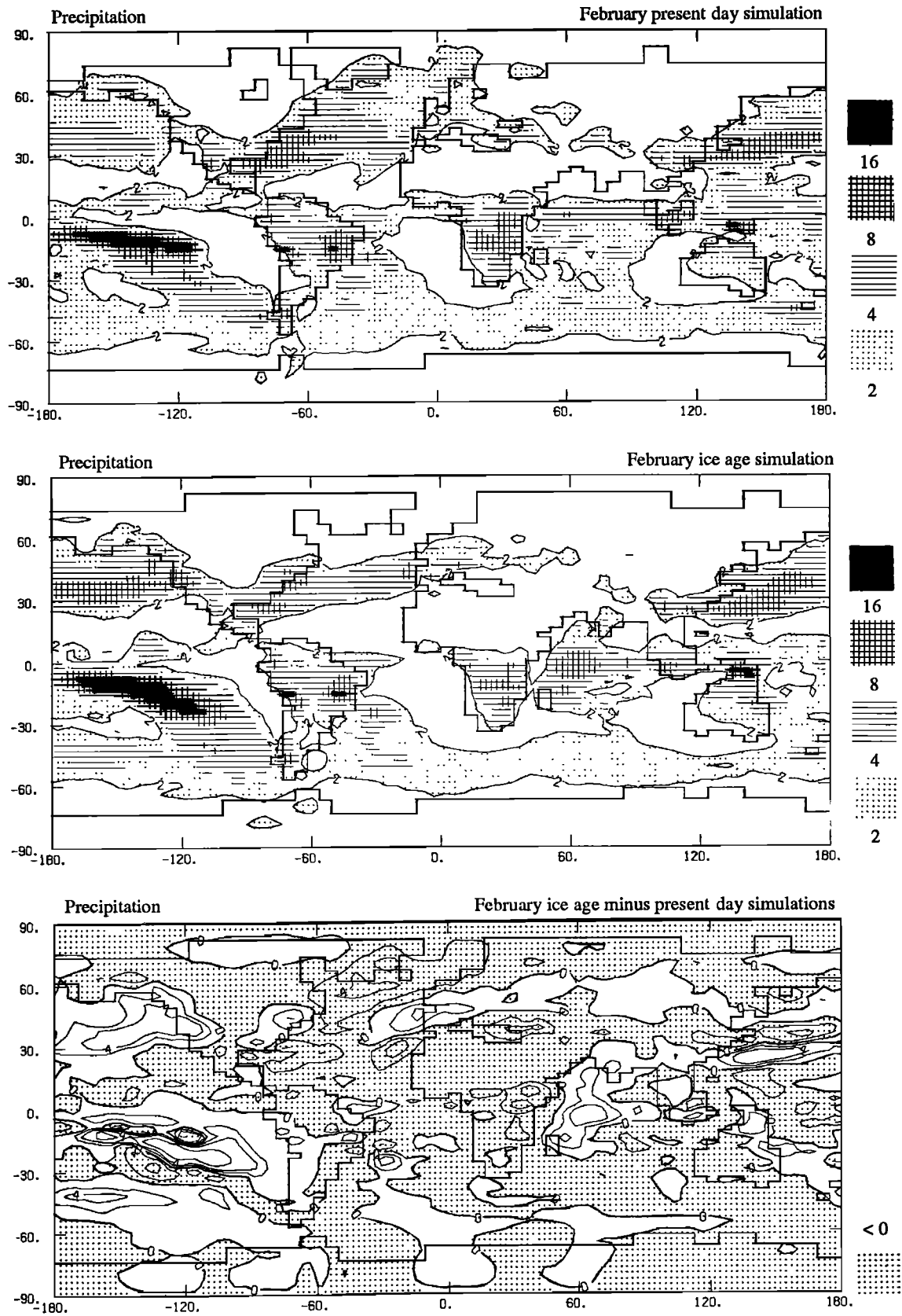


Fig. 8. Simulated precipitation rates in millimeters for the (top) February present-day, (middle) ice age and (bottom) ice age minus present day simulations. Shaded areas are 2, 4, 8, 16 and the isoline is 2 mm d<sup>-1</sup>. The difference field has been smoothed following the procedure of Figure 4, and isolines are 0, ±2, ±4 and ±8 and dotted areas correspond to negative values.

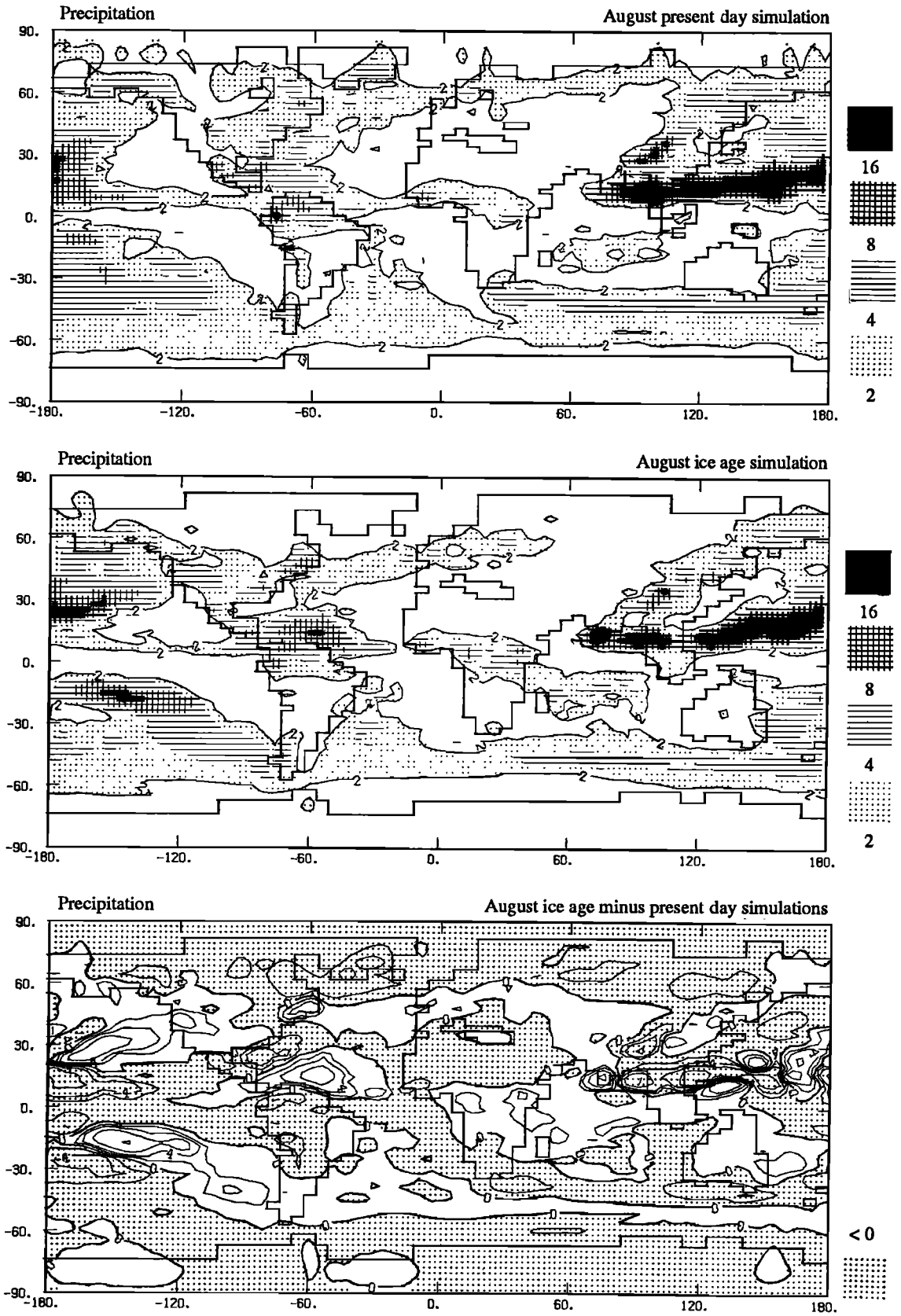


Fig. 9. Same as Figure 8 but for August.

these latitudes (Figure 7), especially over the continents thanks to their smaller thermal capacity compared to the oceans. The land-ocean thermal contrast is thus modified and yields changes in the NH atmospheric circulation. During the winter season, the land-ocean thermal contrast is increased. The continental highs are strengthened (Figure 5) in association with an intensified sinking of cold dense air. Anticyclonic circulations are simulated over North America and Eurasia. In the summer season, the land-ocean contrast is decreased and the continental lows are weakened, e.g., the thermal Asian Low (Figure 6).

Another important change in the boundary conditions is the strong southward expansion of the North Atlantic sea ice (Figure 1). Sea ice favors an important cooling and cuts off the oceanic source of latent and sensible heat fluxes. In February, the strongest temperature decrease is simulated in this area with values over 35°C (Figure 7). The cooling over sea ice is particularly strong compared to the bordering ice sheets since it is not associated with a change in surface elevation. It reflects important changes in the atmospheric circulation. The storms originating in the Gulf Stream region no longer extend over the northeast Atlantic Ocean. Precipitation strongly decreases in this region (Figure 8) and a high pressure develops (Figure 5). Storms remain confined to the southern margin of the sea ice cover and extend toward southern Europe, as can be seen from the sea level pressure (Figure 5) and precipitation (Figure 8). Instead, the cyclonic activity is reinforced in the northern Pacific with an important deepening and expansion of the Aleoutian Low, particularly over the northeastern Pacific (Figure 5). Strong low-level westerlies associated with the deeper Aleoutian Low (Figure 5) favor a strong evaporation over the relatively warm ocean waters of the northern Pacific (Figure 1). Free of ice and remaining relatively warm, the Pacific can be an important source of energy for the NH middle latitudes.

In the summer season, in August, the sea ice cover still expands over much of the North Atlantic (Figure 1) and induces trends relatively similar to the winter season, although with a weaker amplitude. A high-pressure pattern develops over the Baffin Bay (Figure 6) and precipitation is confined to the southern margin of the sea ice (Figure 9). The Aleoutian Low deepens at the expense of the subtropical high in the northeastern Pacific (Figure 6) and favors a strong increase in precipitation. The latter leads to the wetter climate of the western coast of North America (Figure 9).

*The midtropospheric circulation.* The changes in the midtropospheric circulation can be discussed in terms of the 500-hPa geopotential height (Figures 10 and 11) which reflects the wind field through the geostrophic equilibrium. The narrowing of the geopotential isocontours indicates an intensification of the tropospheric jet over the Pacific and over Europe for both seasons. This change is consistent with the increased meridional temperature gradients over these regions (Figure 7).

In February, the 500-hPa geopotential height (Figure 10) displays a planetary wave structure which is quite realistic for the present-day climate. The ridge associated with the Rocky Mountains is particularly well reproduced, but the model overestimates the trough located over Europe. This overestimation is not just transient since it is confirmed by other winter simulations performed with the LMD model [Michaud, 1990]. This feature tends to produce northwesterly winds over western Europe for the present-day climate.

The planetary wave structure is strongly modified during the

ice age (Figure 10). Orography and diabatic heating are important forcings of the stationary waves of the northern hemisphere winter, as was demonstrated by the numerical experiments performed by Held [1983]. Orography tends to force an anticyclonic circulation, i.e., a ridge in the geopotential height. A ridge is also induced by a diabatic heating. During the LGM, the Laurentide ice sheet strongly modifies the orographic forcing over North America. In the model, the anticyclonic circulation is no longer restricted to the western side of the continent but expands over the whole continent. The flow is split around the Laurentide ice sheet and a polar jet is formed north of the ice sheet with wind speeds up to 20 m s<sup>-1</sup>. The downstream trough of the wave train generated by this orographic forcing is displaced toward the east. The associated change from northwesterlies to westerlies over northeastern North America leads to the warming pattern of the surface air temperature (Figure 7). The northwesterlies associated with the downwind trough are either channeled between the Laurentide and Greenland ice sheets or pass round Greenland. Cold winds then blow over the North Atlantic and favor the formation of sea ice. Sea ice, in turn, leads to the formation of a trough by cutting off the surface sensible heat flux and by inhibiting storm activity. The North Atlantic storm tracks are indeed shifted toward the southern edge of the sea ice, as is indicated by precipitation (Figure 8). Moreover, the cyclonic activity is weakened over the Gulf Stream by the change in circulation. During the LGM, southwesterly winds replace the present-day cold and dry northwesterly winds blowing from the continent, and therefore weaken the strong evaporation flux located over the Gulf Stream. As a consequence, the North Atlantic ridge of the present-day 500-hPa geopotential height completely disappears during the ice age.

A slight ridge is produced over southern Europe which is probably due to the diabatic heating associated with the storm tracks. But, surprisingly, over northern Europe, no anticyclonic circulation is associated with the orographic forcing of the Fennoscandian ice sheet. As a possible explanation, the Fennoscandian orographic forcing could be counterbalanced by the downwind trough generated by the Laurentide and Greenland ice sheets. The two opposite trends could then lead to the very straight structure of the 500-hPa geopotential height over northern Europe. Over the Pacific, the eastward expansion of the Aleoutian Low displaces the diabatic heating toward the North American coast and, probably, reinforces the North American ridge.

The simulations of the LGM climate performed by other AGCMs (the National Center for Atmospheric Research (NCAR) AGCM [Kutzbach and Guetter, 1986], the Goddard Institute for Space Studies (GISS) AGCM [Rind, 1987], the Max Planck Institut für Meteorologie (MPIM) AGCM [Lautenschlager and Herterich, 1989, 1990] and the Geophysical Fluid Dynamics Laboratory (GFDL) AGCM [Manabe and Broccoli, 1985; Broccoli and Manabe, 1987]) also produced an anticyclonic trend over the Laurentide ice sheet and a splitting of the jet stream. The significant impact of the mechanical effect of the ice sheets over the ice age circulation was also clearly demonstrated by the sensitivity experiments performed by Rind [1987] and by the analyses conducted by Cook and Held [1988] using a linear model. However, the amplitude and location of the changes may differ from one model to the other. For example, the LMD AGCM locates the maximum increase in the 500-hPa geopotential

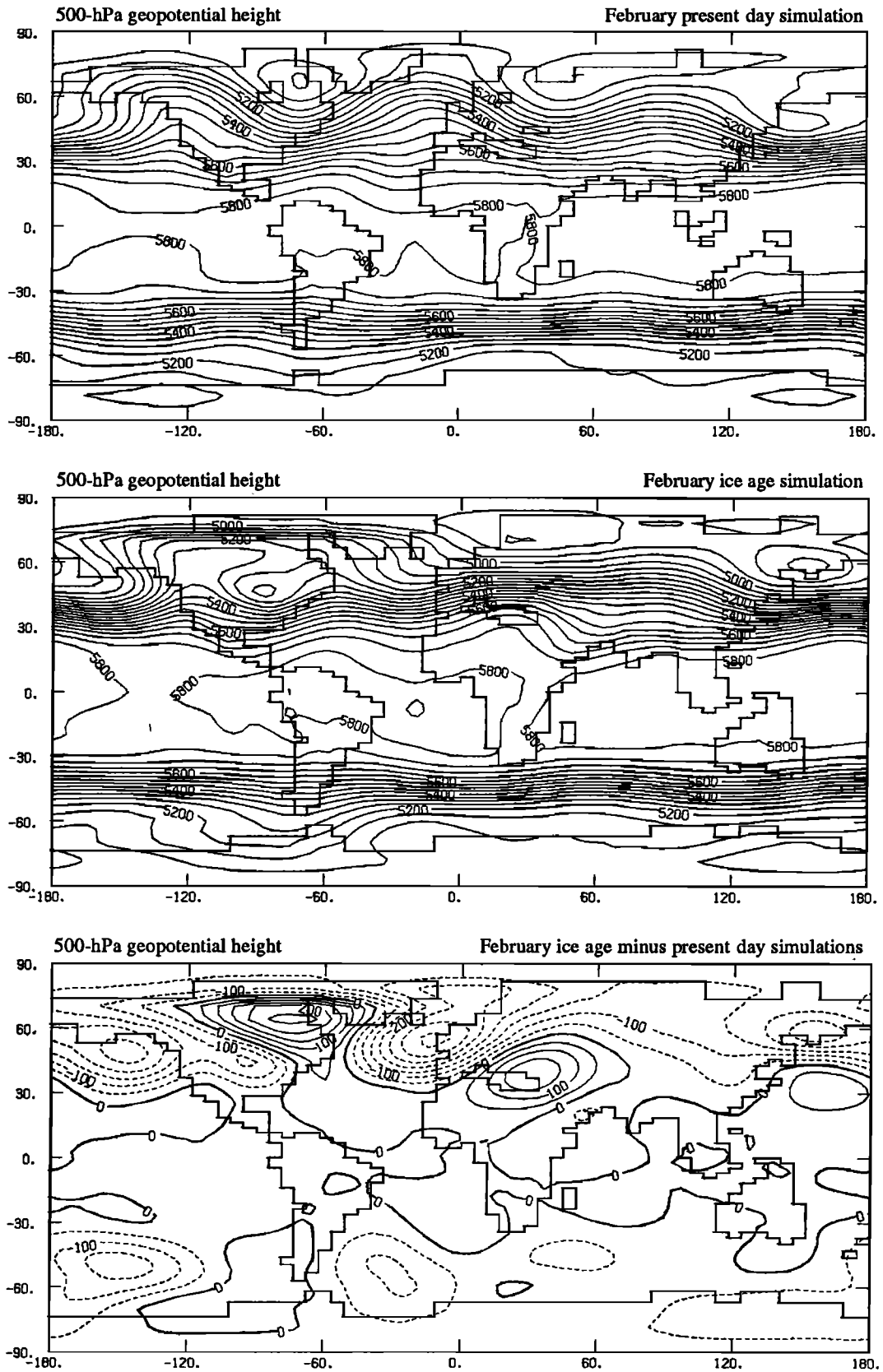


Fig. 10. Simulated 500-hPa geopotential height (meters) for the (top) February present day, (middle) ice age and (bottom) ice age minus present-day simulations. Isolines are at every 50 m and dotted lines drawn for negative values.

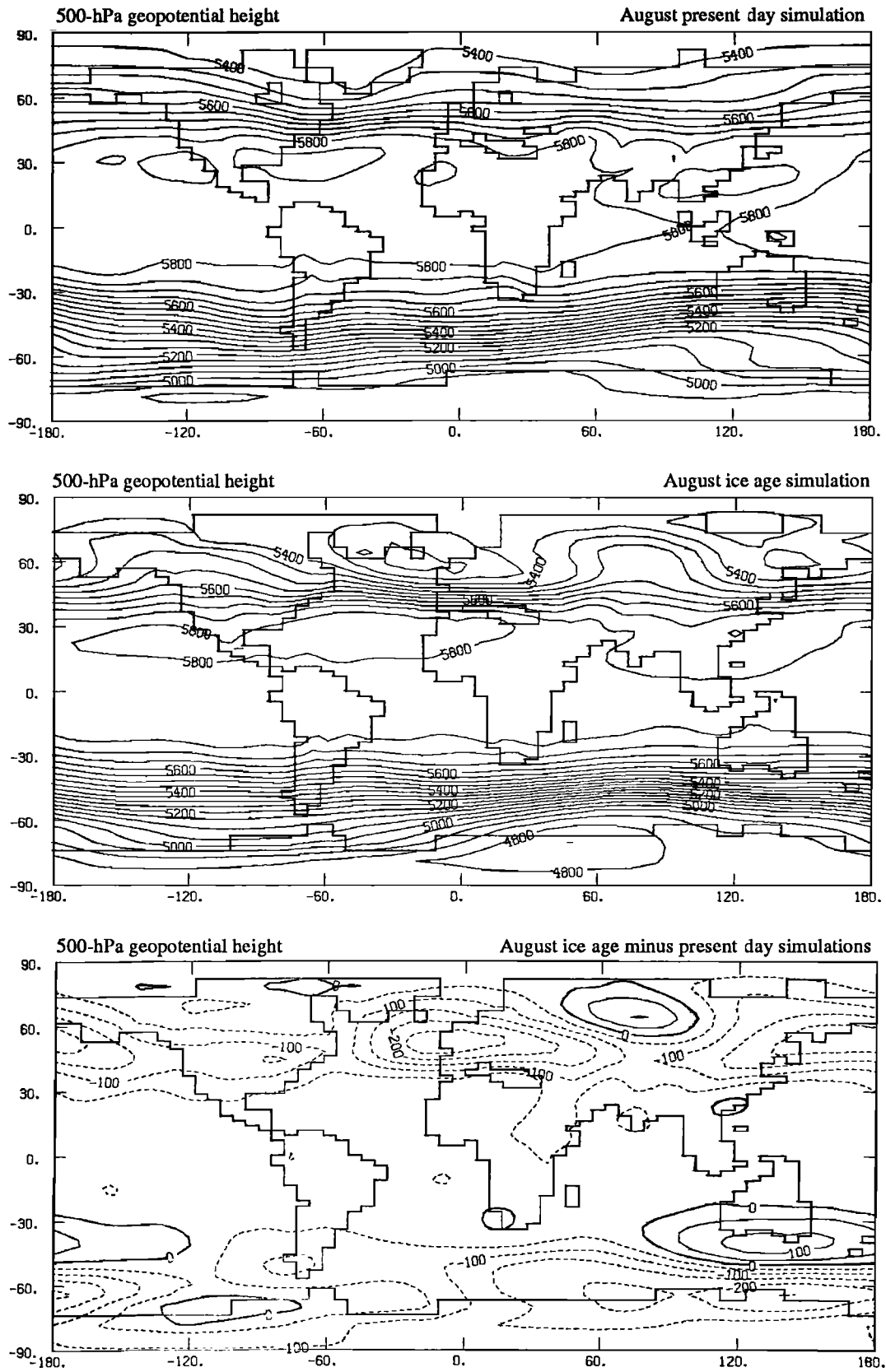


Fig. 11. Same as Figure 10 but for August.

height (i.e., an anticyclonic circulation) farther east than in all the other models for unknown reasons.

The differences between the various AGCM simulations of the ice age are even more important when we compare the simulated atmospheric circulations over Europe. The model results can be separated into two different types of circulations for the ice age: on the one hand, a strong anticyclonic circulation associated with dry and cold northeasterlies, and, on the other hand, storm tracks penetrating over Europe associated with strong westerlies and wetter conditions. The first type of circulation corresponds to the GISS AGCM, whereas the second type corresponds to the LMD and GFDL simulations. The NCAR and MPIM AGCMs lie in between with storm tracks penetrating only over western Europe. Unfortunately, up to now, climatic estimates from paleoclimatic data are insufficiently clear to discriminate between the two types of circulations. Pollen data and lake levels give opposite changes in hydrology for the southern Europe-Mediterranean region (section 4.2) and changes in surface air temperature are not well correlated with the two types of circulations to be used to discriminate between the various simulations.

The planetary wave structure is much weaker in summer than in winter for the present-day climate (Figure 11), in agreement with observations [Oort, 1983]. During the LGM, however, the summer planetary wave structure is strongly amplified with an important trough generated over the North Atlantic. Similar to what occurs in February, the sea ice cover strongly inhibits the local sources of energy. The Icelandic low disappears and is replaced by a high pressure (Figure 6). Instead, the Pacific low is strengthened at the expense of the Pacific subtropical high and induces a ridge of the 500-hPa geopotential height over the western coast of North America. These changes lead to a wave 2 pattern. Below the ridge over central Asia a surface warming is simulated (Figure 7) which results from a southerly advection of warm air associated with the low-level cyclonic circulation located over Europe (Figure 6). For both the NH winter and summer seasons, the increased stationary waves allow the transportation of more energy toward the north pole during the LGM climate and compensate for the higher deficiency of energy resulting from the sea ice expansion and glacial ice sheets.

### 5.3. Southern Hemisphere Extratropical Circulation

The changes in the southern hemisphere (SH) atmospheric circulation are weaker than in the NH extratropical regions. They are mainly governed by the sea ice expansion (Figure 1) and the associated increase in the meridional temperature gradient (Figure 7). Through the thermal wind equation, the westerly winds are increased, but only below 200 hPa and essentially in August (Figures 10 and 11). The cyclonic activity is slightly increased in the roaring forties as seen from the zonal averaged variance of the sea level pressure [Joussaume, 1989]. However, this increase is small for both seasons and mostly within the model variability deduced from other LMD AGCM simulations.

The main change concerns the circulation patterns simulated south of Australia in August (Figure 6). The model produces a systematic deep low pressure in this area. For the present-day climate, this low is overestimated compared to observations [Joussaume, 1990]. During the ice age, the low is weakened and displaced further south. This feature is

significant since it is stronger than the model variability in this area and is persistent during all the simulation. This change has a strong impact on the transport of dust from Australia (section 7).

## 6. THE SIMULATED DUST TRANSPORT FOR THE LGM

The introduction of a dust cycle within the AGCM allows the simulation of the interactions between the atmospheric circulation and the dust transport for both the present-day and LGM climates.

### 6.1. Global Changes in the Dust Cycle

The model predicts a weak change in the global atmospheric dust content for the LGM, with an annual mean increase of only 8% (average of February and August results). The increase is more important in February, with 23%, compared to August, with 1% (Table 3). During the LGM, the seasonal contrast is thus weakened compared to the present-day climate for which the model predicts twice as much dust in August as in February [Joussaume, 1990]. Changes in the atmospheric dust content can result from various processes: changes in the source regions, the dust mobilization flux, the removal intensity and the transport. These processes are all affected by the changes of the atmospheric circulation.

The weak simulated change in the dust atmospheric content for the LGM is in great part determined by the weak changes in the source region extent. The area of the source regions increases by 18% and the source intensity by 14%. The change in source area is deduced from the change in the simulated tropical aridity, since the model predicts the source regions from the simulated dry regions for both seasons. The source intensity is not only dependent on the source extent but also on the surface wind speed. The mobilization flux increases by 25% in February and 7% in August (Table 3). Compared to the 18% change in the source area, these changes indicate a stronger efficiency of the surface winds over desert regions in February and a weaker one in August. The seasonal contrast of the source intensity is therefore weakened during the LGM with an August/February ratio of 1.24 (Table 3) against 1.43 for the present-day climate [Joussaume, 1990].

The amount of dust in the atmosphere also depends on the lifetime of the particles. This latter is defined as the ratio of the dust atmospheric content over the removal flux (Table 3). For the present-day climate, the simulated atmospheric dust content is larger in August than in February, leading to a longer lifetime in August (4.7 days) than in February (3.1 days). Joussaume [1990] emphasized that this longer lifetime in August derives from seasonal changes in the vertical structure of the dust plumes. In August, the vertical ascent of dust is stronger than in February, thus weakening the contribution of the surface dry removal process relative to the tropospheric wet removal process. Since the wet process is less efficient than the dry one in removing dust from the atmosphere in our simulations, the lifetime is increased in August.

During the LGM climate, the atmospheric dust content essentially increases in the planetary boundary layer (PBL) for both seasons. This increase is achieved at the expense of the free tropospheric amount (TR) in August (Table 3 and Figure 12). The change in the vertical structure enhances the efficiency of the dry removal intensity (Table 3). In August,

TABLE 3. Global Budgets of the Simulated Atmospheric Cycle of Desert Dust Particles for February and August Ice Age and Comparison With the Results of the Present-Day Climate

	Surface Area	$S_p$ kgAU $m^{-2} d^{-1}$	$M_p$ kgAU $m^{-2}$	$R_{Wp}$ kgAU $m^{-2} d^{-1}$	$R_{Dp}$ kgAU $m^{-2} d^{-1}$	$\tau = M_p / S_p$ days	$\partial M_p / \partial t$ kgAU $m^{-2} d^{-1}$
<i>February Ice Age</i>							
Global	176 points	38.5	119.5 PBL= 81.7% TR = 18.3%	-6.1	-32.5	3.1	-0.1
Sahara	44.9%	33.2%	36.5%	28.3%		3.4	
Arabia-Asia	37.5%	38.7%	37.2%	38.8%		3.0	
North America	1.7%	3.8%	2.3%	4.4%		1.9	
Australia	6.8%	11.4%	11.6%	12.1%		3.2	
South America	4.55%	7.3%	5.8%	8.8%		2.4	
South Africa	4.55%	5.6%	6.6%	7.6%		3.7	
<i>February Ice Age / February Present Day</i>							
Global	1.18	1.25	1.23 PBL= 1.27 TR =1.08	1.10	1.28	0.99	
Sahara	1.20	1.20	1.07	0.98		0.89	
Arabia-Asia	1.14	1.26	1.43	1.07		1.13	
North America	1.50	1.77	1.94	1.82		1.10	
Australia	1.33	1.57	1.50	1.50		0.95	
South America	1.14	0.94	0.87	0.98		0.93	
South Africa	1.14	1.16	1.15	1.20		0.99	
<i>August Ice Age</i>							
Global	176 points	47.6	209.5 PBL= 57.8% TR = 42.2%	-11.4	-36.0	4.4	0.2
Sahara	44.9%	38.4%	49.2%	40.7%		5.6	
Arabia-Asia	37.5%	40.9%	38.6%	49.8%		4.1	
North America	1.7%	2.2%	1.5%	1.3%		2.9	
Australia	6.8%	8.6%	3.8%	4.0%		1.9	
South America	4.55%	5.3%	2.6%	2.1%		2.2	
South Africa	4.55%	4.6%	4.3%	2.1%		4.2	
<i>August Ice Age / August Present Day</i>							
Global	1.18	1.07	1.01 PBL= 1.10 TR = 0.91	1.16	1.04	0.94	
Sahara	1.20	1.13	0.97	1.11		0.86	
Arabia-Asia	1.14	1.02	1.02	1.24		1.00	
North America	1.50	1.62	1.44	2.29		0.89	
Australia	1.33	1.15	1.25	0.90		1.08	
South America	1.14	0.98	0.79	0.91		0.81	
South Africa	1.14	0.94	1.40	1.06		1.49	

Source area, source intensity  $S_p$ , mean atmospheric vertical content of dust  $M_p$ , wet removal  $R_{Wp}$ , dry removal  $R_{Dp}$ , mean residence time  $\tau$  and balance excess  $\partial M_p / \partial t$ . For  $M_p$  we give the separate contributions for the planetary boundary layer (PBL, first four  $\sigma$  layers of the model) and for the free troposphere (TR, next four  $\sigma$  layers). The global budgets are separated for the different source areas. The definition of the Saharan source can be seen in Figure 22. The global deserts surface areas are given as a number of grid points (each of equal area: 160,850  $km^2$ ) to be compared to a total number of 3200 grid points.

the latter is further reinforced by an enhanced efficiency of the wet removal, which increases by 16% compared to the global atmospheric amount increase of 1%, therefore reducing the lifetime. In February, the change in the dry removal intensity is in great part compensated by the reduced efficiency of the wet removal, leading to a lifetime that is almost unchanged.

This discussion shows that the global amount of dust is highly dependent on the overall atmospheric cycle of the dust from the source to the removal processes and, therefore, is intimately related to the changes of climate. The simulated results should also be dependent on the parameterizations used for the dust modeling, but specific sensitivity experiments were not performed in this first approach due to the high cost of each run. For example, changes in the source intensity are

certainly sensitive to the surface wind speed function used for the dust mobilization flux.

We are also concerned with the relatively short time length of our experiments. The first forty days of simulations are dropped in order to reach a global equilibrium of the dust cycle during the period of analysis (Figure 12). We then consider averages over the last 60 days of the numerical experiments. This time scale is large compared to the lifetime of the dust particles (of the order of 5 days) and allows a good representation of the dust cycle, but it is not long enough to capture the low-frequency variability of the atmospheric circulation. It may thus bias the simulated results for the dust cycle. The 60-day period appears well representative of the global changes in the source intensity and the atmospheric dust content (Figure

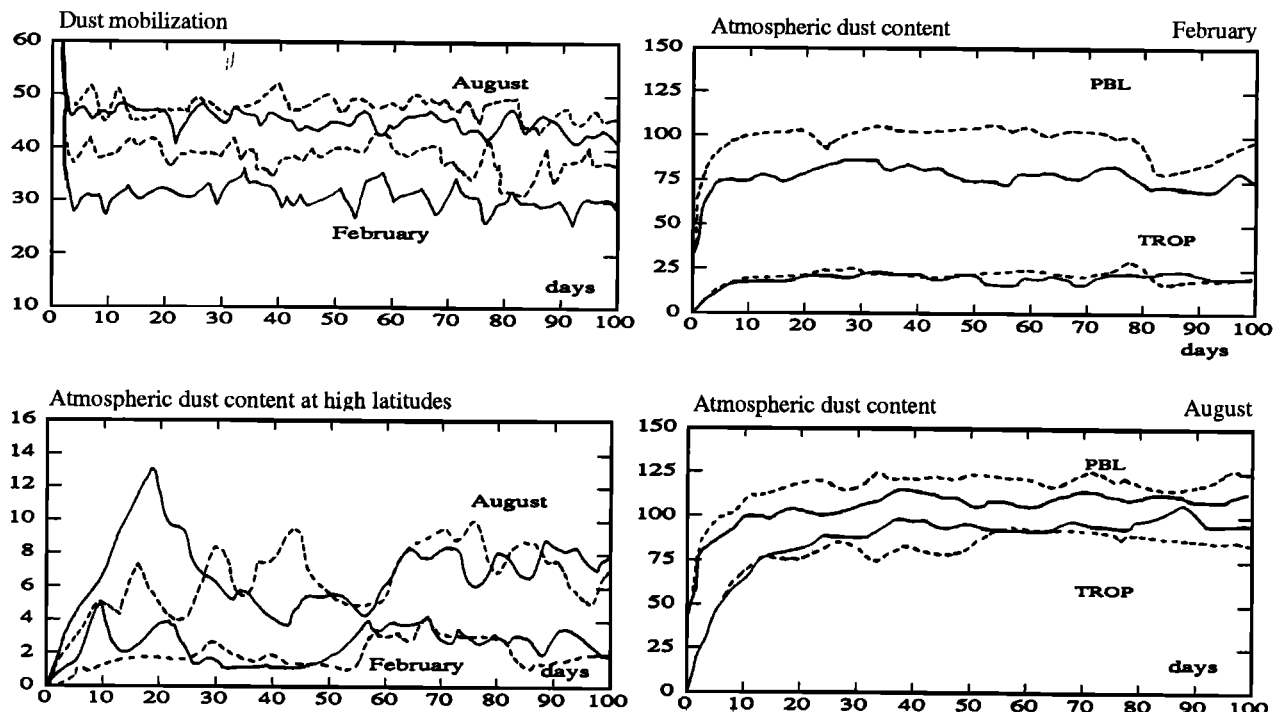


Fig. 12. Time evolution of the global averages of the dust mobilization  $S_p$  ( $\text{kgAU m}^{-2} \text{d}^{-1}$ ), of the atmospheric dust content ( $\text{kgAU m}^{-2}$ ) vertically integrated over the planetary boundary layer (PBL) and the free troposphere (TR), and of the vertically integrated dust mass ( $\text{kgAU m}^{-2}$ ) averaged over the only high latitudes ( $60^\circ\text{N}$ - $90^\circ\text{N}$  and  $60^\circ\text{S}$ - $90^\circ\text{S}$ ) for (solid line) the February and August present-day and (dashed line) the ice age simulations ( $\text{kgAU}$ : dust mass in arbitrary units).

12), but the short frequency variability of the atmospheric circulation is more sensitive at a regional scale as can be seen from the high-latitude atmospheric dust content (Figure 12) and as was discussed by Joussaume [1990].

## 6.2. Regional Features

The simulated changes in the global mean atmospheric dust cycle are weak for the LGM, but changes can be more important regionally. We focus first on the annual mean results which are more comparable to paleoclimatic data and which account for the relative contribution of each season. We will then consider the results for each season to better emphasize the impact of the atmospheric circulation changes on the desert dust cycle.

**Source regions.** Source regions for the present-day and ice age climates are shown in Figure 13. The Saharan source, which includes all sources located over the Sahara, the Horn of Africa and southern Europe, is the strongest source of dust in the model (Table 3). During the LGM, its area increases by 20% by an expansion toward the south of the Sahara and southern Europe. The Arabian-Asian source, the second one in size, expands over Arabia and toward eastern India. Some sources shrink in the Turkmenia steppes. In North America, the sources expand toward Mexico. In the southern hemisphere, a one-grid-point source vanishes in the Atacama desert, whereas sources appear in the Gran Chaco steppes. In southern Africa, the sources essentially expand toward the north. The Australian source increases by 33% and moves southward, especially in the southeast.

To test the reliability of the simulated changes in the source regions, we can use the fossil dune records of Sarnthein [1978]. The simulated changes are in general fairly well

corroborated by past data, in particular the Gran Chaco source and the expansion of the Saharan and Australian sources toward the south. The southeastern sources in Australia are also in good agreement with the results of Bowler [1977]. However, the simulated expansion of the Sahara southward is limited to 200 km, compared to an estimate of 500 km [Rognon, 1980]. No expansion toward the interior of the continent is obtained for the south African source, in contradiction with fossil dune records. Therefore, the model seems to underestimate the increase of desertic areas during the glacial maximum.

**Changes in the atmospheric dust content.** If the changes are practically negligible on the global scale, the increase can reach a factor of 2 to 10 over the northwestern Atlantic Ocean, Europe and southeast of Australia (Figure 14). More dust is transported over these regions during the LGM either because of an increased extent of the source regions, like in Mexico, southern Europe and southeast Australia, or because of changes in the atmospheric circulation (or both processes). The vanishing of grid point sources is also made clearly visible north of the Atacama and south of Africa by a strongly reduced dust amount.

**Dust removal flux.** Changes in the dust removal (Figure 14) follow in great part the simulated changes in the atmospheric dust content. Some differences between the two fields are, however, displayed. Near the source regions, the differences are essentially related to changes in the dry removal flux (Figure 14), as for example over the equatorial Atlantic Ocean and over the Indian Ocean. They result from increased surface winds and/or changes in the vertical distribution of dust, since dry removal only involves surface concentrations. Farther from the source regions, the wet removal process prevails [Joussaume, 1990]. The changes in the amount of precipitation (Figure 4) control the changes in the dust removal,

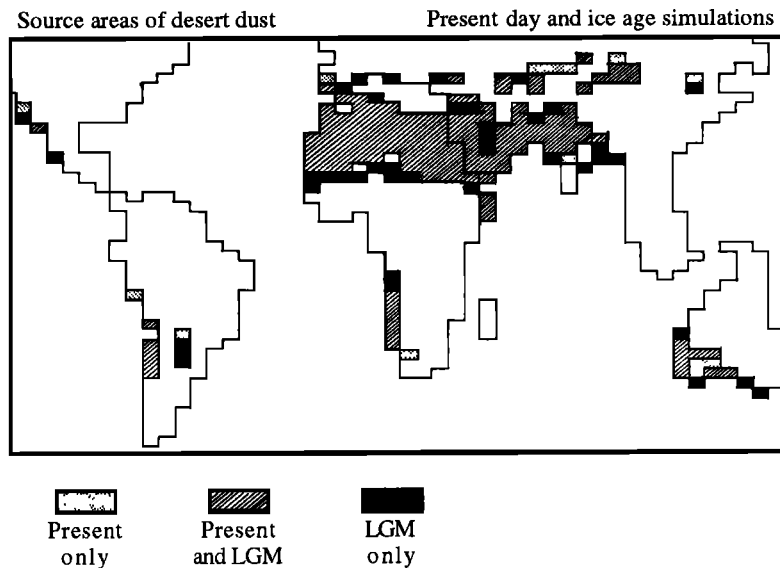


Fig. 13. Simulated source areas of desert dust, defined as the regions that are dry in February and in August, for the present-day and ice age simulations. Dotted areas correspond to sources for the present-day only, solid areas for the ice age only and hatched for both climates.

especially in the northeast Pacific, the eastern Sahara and the Indian Ocean, where the changes in the atmospheric content are weak (Figure 14).

The annual mean change in the total removal flux of dust must be used to compare the simulated results to paleoclimatic data from ice cores and deep-sea sediments. This comparison will be discussed in section 7, but we can see right now that the model does not simulate any large increase in the dust deposits at high latitudes, conversely to what ice cores tell us.

### 6.3. Seasonal Changes

The simulated desert dust cycle indicates a well-marked seasonal dependency for the present-day climate [Joussaume, 1990]. The changes occurring during the LGM climate also differ from one season to the other. In February (Figure 15), the regions of increase in the atmospheric dust load and dust removal flux are more extended than in August (Figure 16). The North Atlantic-European sector, which experiences the most important increase, also exhibits different patterns which are associated with specific seasonal changes in the atmospheric circulation. Changes in this sector are mostly governed by the Saharan and Arabian-Asian dust sources.

**Saharan dust.** The transport of Saharan dust is strongly affected by the changes in the atmospheric circulation in February (Figure 17). Over the source regions, the transport of dust is very sensitive to the strong high pressure developing over the eastern Mediterranean Sea (Figure 5) which is one of the major changes in the February LGM low-level circulation (section 5). During the LGM, dust is then preferentially transported southwestward of the Sahara and toward southern Europe (Figure 17), rather than eastward and over the North Atlantic as is simulated for the present-day climate [Joussaume, 1990]. As a consequence, the atmospheric dust load is much decreased eastward of the Sahara and over the North Atlantic and is enhanced over Europe and the tropical Atlantic, all changes lying within ratios of 2 to 5 (Figure 17). Over the Atlantic, the dust transport is also influenced by the changes in the Açores High, which is stronger and more confined to tropical latitudes during the LGM. However, this

last feature is in great part transient. Indeed, the present-day 60-day mean simulated February climate is characterized by a blocking situation which is associated with a too weak Açores High and a high located over southwestern Europe (Figure 5), and therefore corresponds to an important northward transport of dust over the North Atlantic [Joussaume, 1990].

During the summer season, the source and transport of Saharan dust is more important than during the winter season. For the present-day climate, the transport occurs essentially westward, over the Atlantic, and eastward, by the low-level monsoon winds [Joussaume, 1990]. During the LGM, the eastward transport is reduced by about a factor of 2 (Figure 18) as a result of the weaker monsoon winds (Figure 6). Conversely, the westward transport is enhanced since it is favored by stronger sources in the western Sahara and by stronger trade winds, this last feature being barely significant. The stronger transport toward Europe results from new sources located in southern Europe as well as from a displacement of storm tracks over southern Europe which allows a transport of Saharan dust by transients (Figure 18). An important increase in the atmospheric dust load is also simulated north of Europe as a result of the low-level cyclonic circulation simulated there, which also favors a transport of Saharan dust, as well as Arabian-Asian dust (Figure 20), toward Greenland during the LGM.

**Transport of Arabian-Asian dust.** Arabia-Asia is the second major source of dust after the Sahara (Table 3). The transport of dust from Arabia-Asia also contributes to the increase in the dust amount over the Atlantic and Europe during the LGM (Figures 19 and 20), but this contribution is less than the Saharan one for both seasons (Figures 17 and 18). Changes in the transport of dust from Arabia-Asia affect the amount of dust over the Indian Ocean and the western Pacific. In August, changes in the Asian monsoon wind regime induce a reduced transport of dust toward the Indian Ocean and western tropical Pacific, whereas in February the transport is increased toward the Indian Ocean as a result of a stronger northerly flow over Arabia, associated with the strong high pressure developing over the eastern Mediterranean Sea. The transport toward the

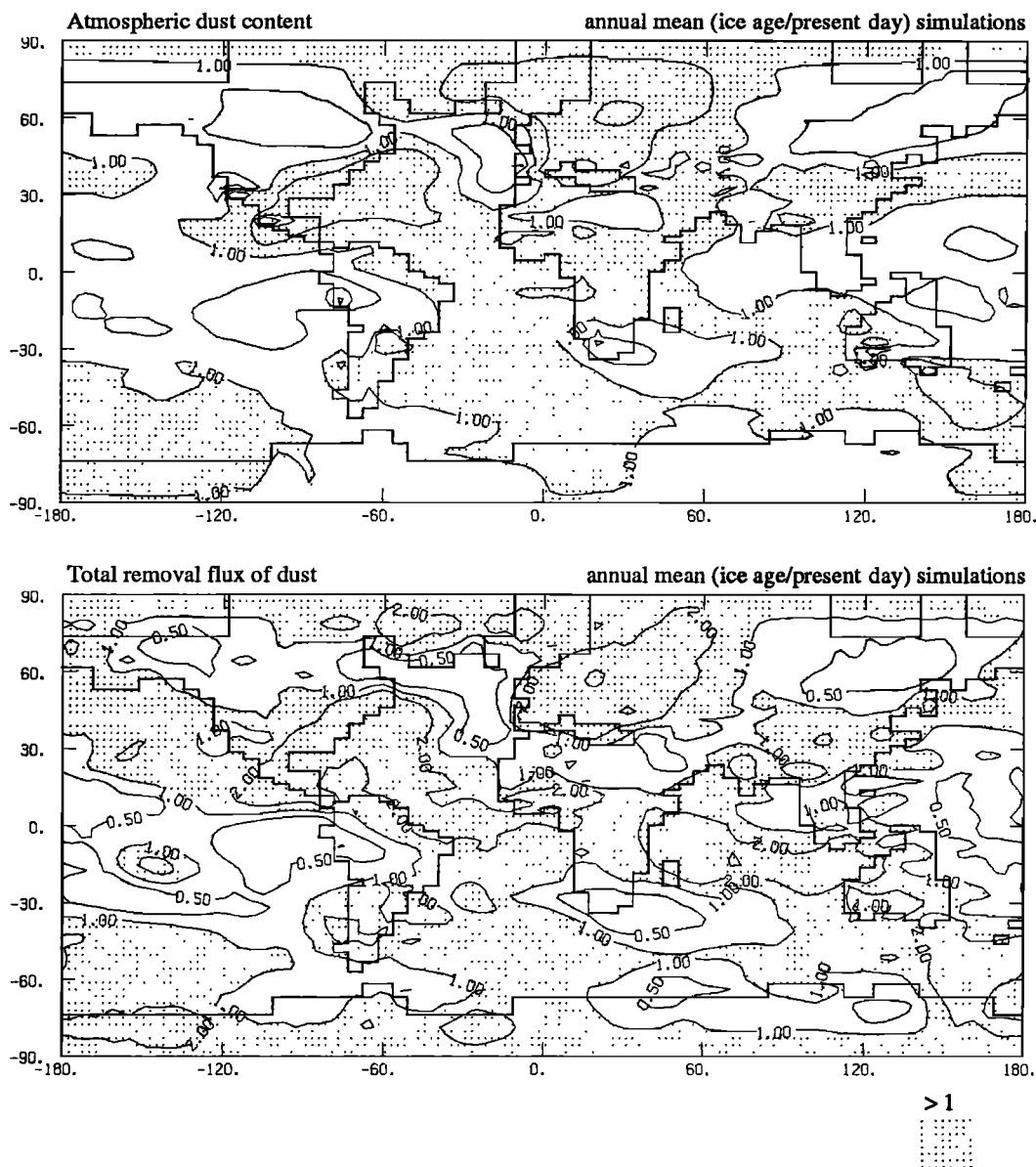


Fig. 14. Annual mean simulated changes in the atmospheric dust content (i.e., the vertically integrated mass of dust,  $\text{kgAU m}^{-2}$ ), and the total, dry and wet removal fluxes ( $\text{kgAU m}^{-2} \text{d}^{-1}$ ). All these ice age over present-day ratios have been filtered following the procedure of Figure 4. Isolines are 1/10, 1/2, 1, 2 and 10, and for the atmospheric dust content the isolines 1/5 and 5 are added. Dotted areas correspond to ratios above 1.

western Pacific is enhanced for both seasons in association with the deepening of the Aleutian Low (Figures 5 and 6).

**Transport from the other source regions.** The other source regions contribute much less to the global changes in the dust cycle during the LGM (Table 3). The simulated changes appear to be strongly determined by the changes in the location of the source areas, as for example in Mexico, the Atacama, the Gran Chaco and southern Africa. A notable change in the dust load occurs in February south of Australia. The transport from the southern hemisphere sources will be further analyzed when discussing the transport of dust toward Antarctica in section 7.

## 7. COMPARISON WITH DUST PALEOCLIMATIC DATA AND DISCUSSION

### 7.1. Transport of Dust Toward Antarctica

**Comparison with paleoclimatic data.** In East Antarctica, in

the area of the Vostok ( $78^{\circ}28'S$ ,  $106^{\circ}48'E$ ) and Dôme C ( $74^{\circ}39'S$ ,  $124^{\circ}10'E$ ) stations, the model simulates a net annual decrease of the total dust removal flux by 0.40 and 0.46 at  $70^{\circ}03'S$  and  $78^{\circ}31'S$ , respectively (Table 4). Conversely, in West Antarctica around Byrd ( $80^{\circ}01'S$ ,  $119^{\circ}31'W$ ) an increase by 2.2 is simulated. This east-west pattern extends over all of Antarctica (Figure 14). In order to compare the simulated results with dust paleoclimatic data from ice cores, we must, however, consider the changes in the dust concentration in snow, i.e., the ratio of the dust removal flux to the snow accumulation rate, rather than the dust fluxes themselves. In the simulated ice age climate, the dust concentration in snow remains practically unchanged in East Antarctica and increases in West Antarctica by only 40% (Table 4). Indeed, at these latitudes, the dust removal flux is in great part controlled by the wet removal process [Joussaume, 1990] (Table 4) and changes in the atmospheric dust content are too weak (Figure 14) to induce a large change in the efficiency of the wet

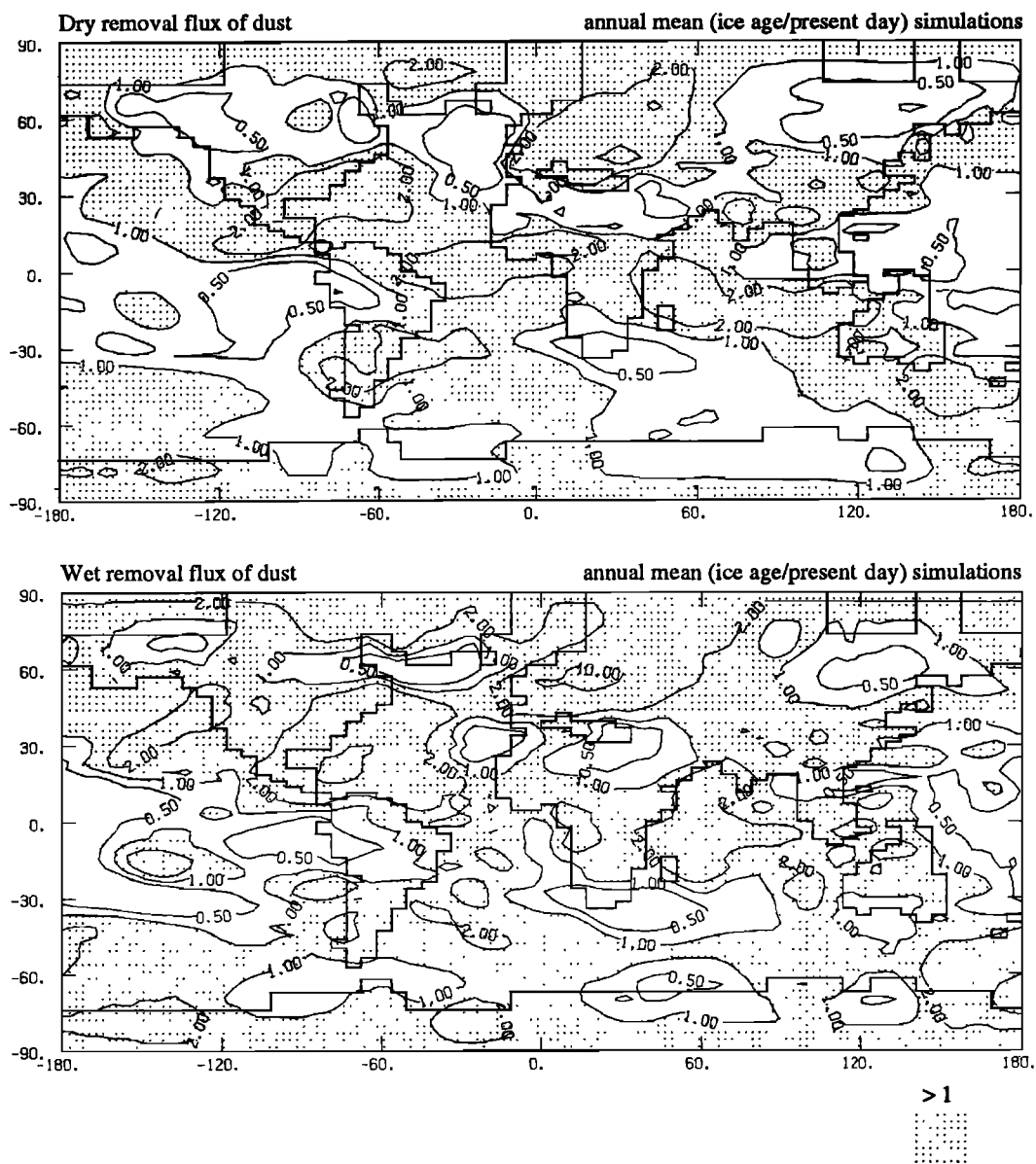


Fig. 14. (continued)

removal process. Nevertheless, the simulated results are far from the observed increases of dust concentration in snow which are of the order of 10 to 20 in East Antarctica and 4 in West Antarctica. To better understand the simulated results, let us consider the seasonal cycle of the desert dust cycle.

*Seasonal dependency.* For the present-day climate, the transport of dust toward Antarctica shows a strong seasonal cycle. Averaged over Antarctica, the dust concentration in snow is about 3 times stronger in August than in February. This seasonal dependency is essentially related to changes in the atmospheric circulation. It results from an increased meridional transport by the transient eddies during the winter season. The intensity of the southern hemisphere sources is also increased during the winter season, but by less than 30% [Joussau, 1990]. The seasonal contrast is even stronger in East Antarctica, in the Vostok and Dôme C areas. The August to February dust concentration ratios take the values of 5 to 4 from the coast toward the interior of the continent (Table 4). This strong seasonal dependency is confirmed at Byrd station

where the model simulates 3 times as much dust in winter as in summer, in very good agreement with an observed ratio of 3 to 4 [Thompson, 1977b]. This last result also validates the use of an annual mean, based on the February and August results only.

During the LGM, the total dust removal flux averaged over Antarctica increases in February and decreases in August, therefore weakening the seasonal contrast and leading to weak annual mean changes (Table 4). In February, the increase concerns the whole continent, whereas the increase is confined to the western side of the continent in August (Figure 21). The changes in the total dust removal flux are in great part determined by the changes in the precipitation rate (Figure 4), although they show a net increase in the dust concentration in snow of the order of 2 over Antarctica (Table 4).

*The origin of dust deposits.* The prevailing transport from the southern hemisphere dust sources of South America, South Africa and Australia is westward, and is associated with the mean westerly circulation of the middle latitudes (Figure 21). In February, dust deposits over Antarctica mainly come from

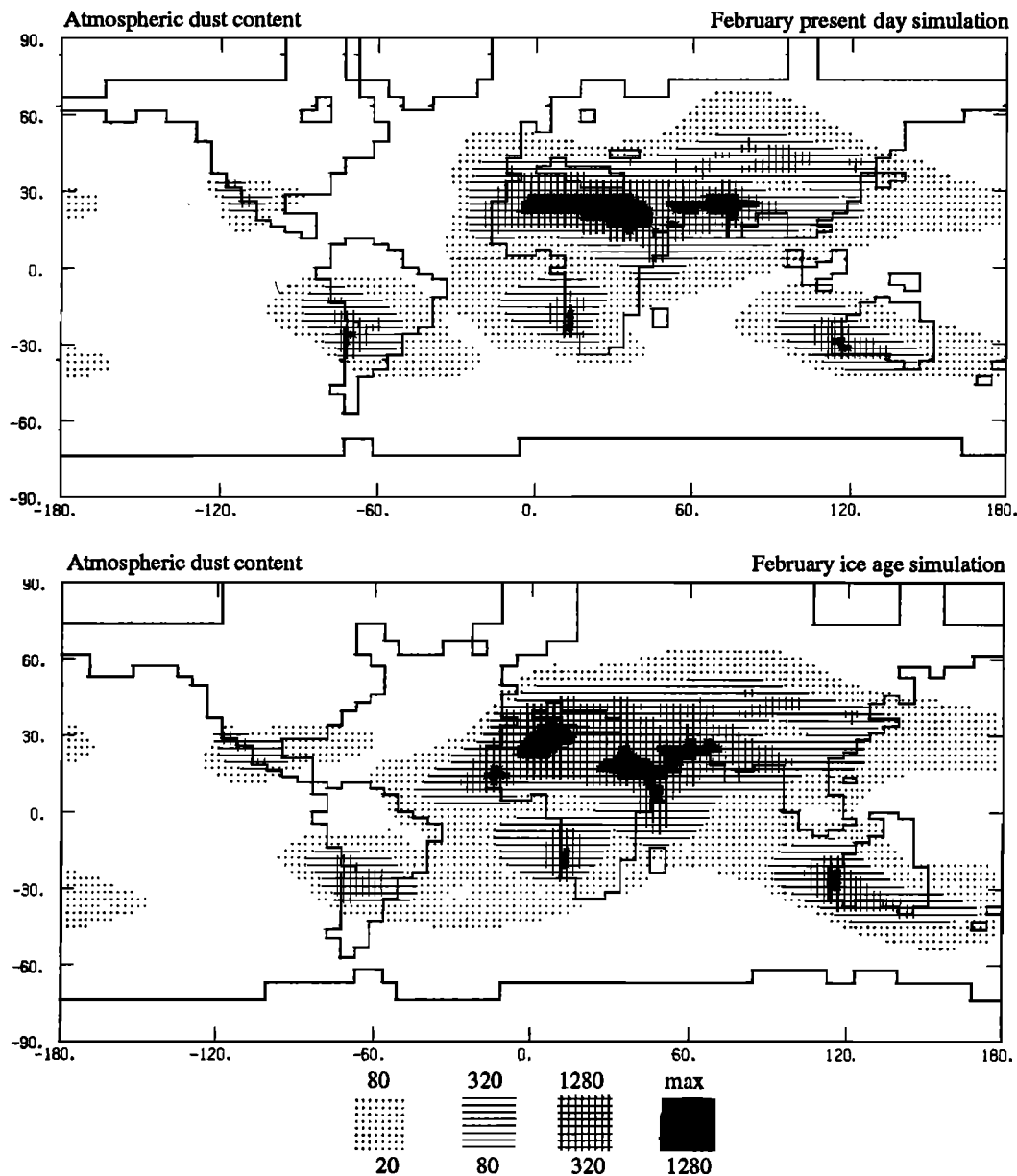


Fig. 15. Atmospheric dust content for the present-day and ice age February simulations ( $\text{kgAU m}^{-2}$ ), and changes in the atmospheric dust content and total removal fluxes. The dust plumes are displayed with shaded areas in a geometrical progression of ratio 4: 20, 80, 320, 1280  $\text{kgAU m}^{-2}$ . The ice age over present-day ratios have been smoothed following the procedure of Figure 4 and are displayed with the isolines 1/10, 1/5, 1/2, 1, 2, 5, 10, with dotted areas for values above 1.

South America and Australia, whereas in August the Australian source is the prevailing one (Table 4). The contribution of the South African source remains weak for both seasons. On annual mean, the Australian source prevails, especially over East Antarctica (Table 4). Therefore, the simulated changes in the dust concentration in snow during the LGM are mainly driven by changes in the transport of dust originating from Australia.

**Changes in the atmospheric circulation patterns.** For the present-day climate, the transport of dust originating from Australia toward Antarctica is particularly strong in August (Figure 22). This feature results from an important dust mobilization in winter by strong surface winds over the continent and from a strong meridional transport by transient eddies. This transport is achieved by the cyclonic activity simulated south of Australia (Figure 6), which tends, however,

to be systematically overestimated in the model [Joussaume, 1990].

During the LGM, the transport of dust originating from Australia is increased in February everywhere above Antarctica. The increase reaches 2 to 5 times the present-day value south of Australia (Figure 22). This tendency results mainly from a southward expansion of the Australian source (Figure 13), as is illustrated by the meridional fluxes of Australian dust in Figure 23.

In August, the atmospheric content of dust originating from Australia decreases during the LGM by a factor of 2 south of Australia and increases further west (Figure 22). During this season, the southward shift of the source areas does not induce a great change in the transport of dust toward Antarctica, since it is compensated by weaker surface winds above the continent (Figure 6), thus decreasing the intensity of the source (Figure

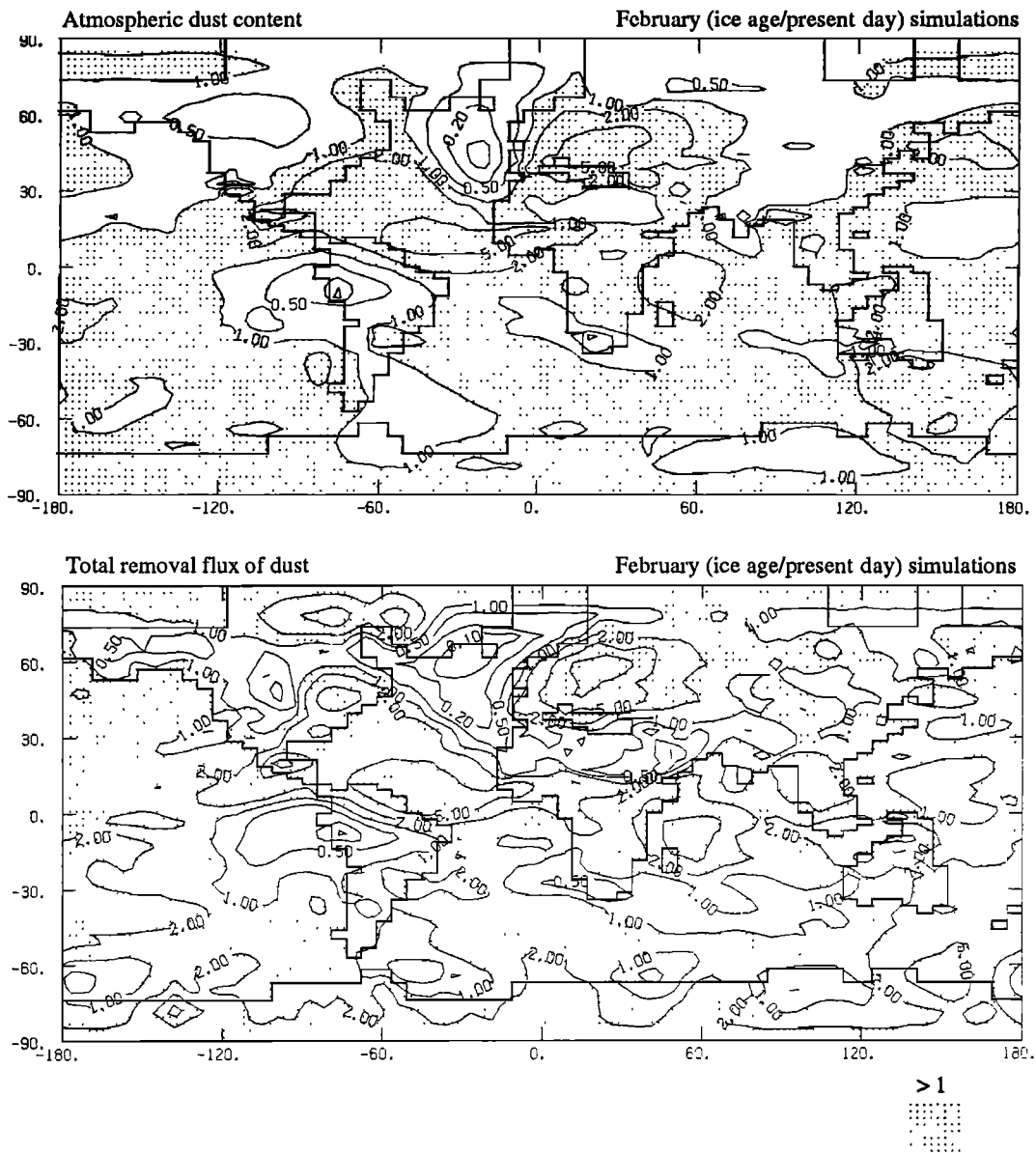


Fig. 15. (continued)

23). Moreover, the meridional transport by eddies is weakened in August LGM (Figure 23), likely a consequence of the weakening of the low located south of Australia (Figure 6). Nevertheless, near Antarctica, this weakening is partially compensated in zonal average by a strengthening of the transport by the mean meridional winds (Figure 23). This last feature corresponds to the poleward displacement of the low located south of Australia. This displacement leads to the maximum atmospheric dust content located southeastward of Australia and to the increase in the dust atmospheric content simulated over West Antarctica during the LGM (Figure 22). All the changes in the atmospheric circulation around Australia are therefore particularly critical to the dust transport toward Antarctica. They are all related to the weakening and poleward displacement of the low located south of Australia in winter. This change appears to be significant since it persists for more than 140 days of simulation, although the location of the Low may vary slightly around Australia. This change is likely to be a consequence of the equatorward expansion of the sea ice margin in this area.

*Discussion.* In our simulations of the LGM climate, the dust concentration in snow remains practically unchanged compared to the present-day climate, in opposition to data from ice cores which show an increased concentration by a factor of 10 to 20. The problem is then to understand what may cause this discrepancy between the simulated results and observations. Several causes may be involved, such as deficiencies in the dust modeling or in the simulated circulation. The latter will be reviewed in the last section of the present paper.

To explain the observed increase in dust concentration in snow over East Antarctica, *Petit et al.* [1981] evoked increases of the source extent and intensity as well as a stronger meridional transport. All three mechanisms indeed contribute to the simulated changes in the dust results. However, they cancel each other, and lead to no net increase in the transport of dust in August, which drives the simulated changes in annual mean for East Antarctica. The importance of the Australian source shown in the model results may, however, be questioned. Indeed, no kaolinite has been observed in the

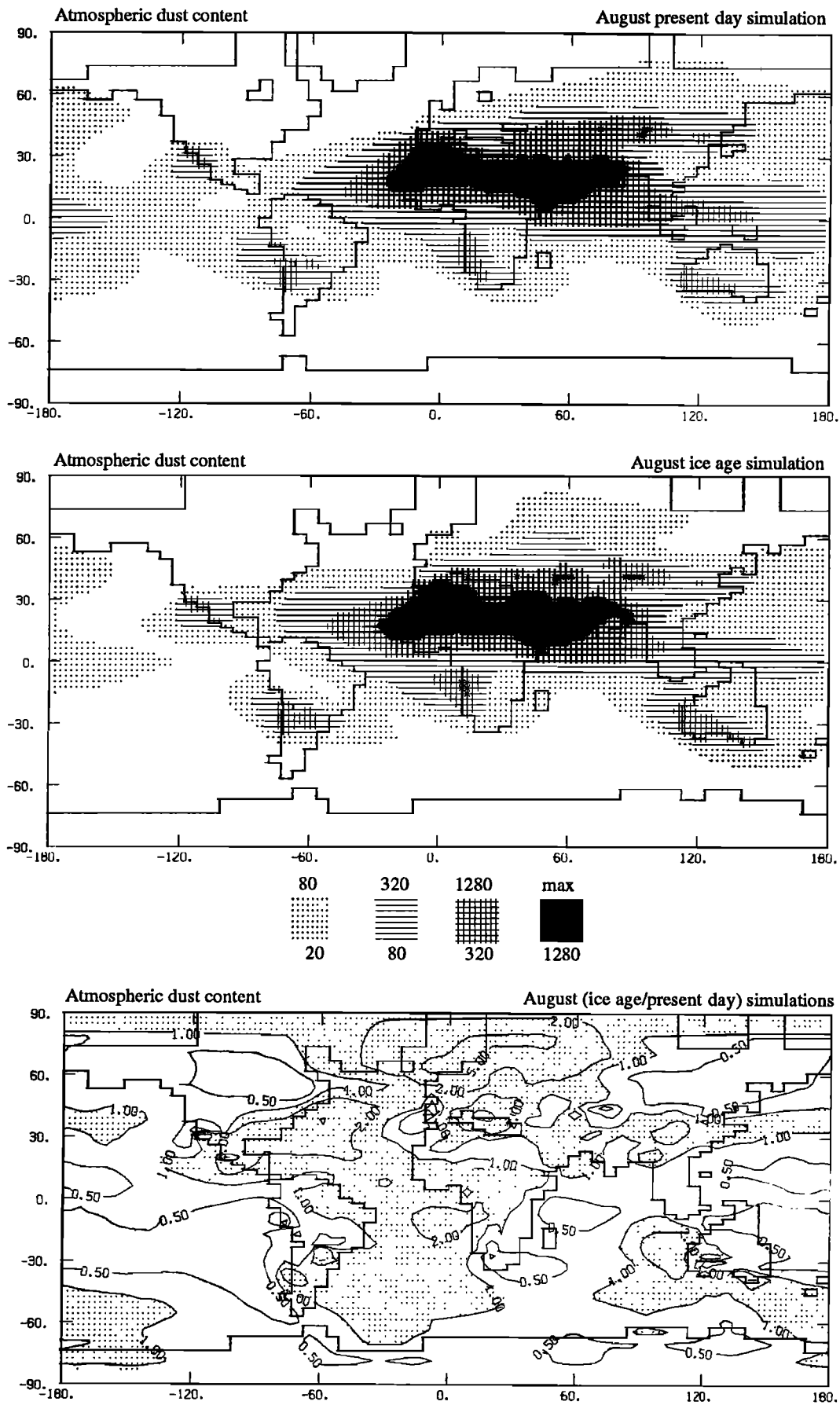


Fig. 16. Same as Figure 15 but for August.

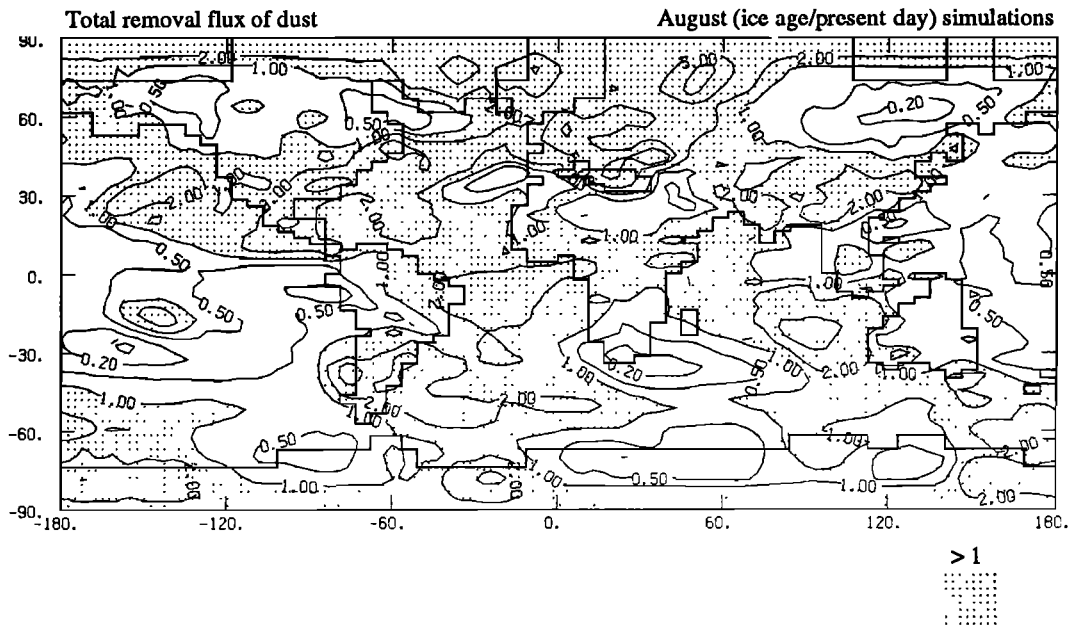


Fig. 16. (continued)

microparticle analyses of the dust deposits of Dôme C and Vostok for the LGM [Gaudichet *et al.*, 1986, 1988, 1992], whereas this type of clay particle is commonly found in the Australian deserts. Australia then does not appear to be the prevailing source of dust deposits during the LGM, unlike what the model suggests. Another source must have contributed to the dust deposits in East Antarctica. During the LGM, dust may come from Patagonia, as has been recently emphasized by isotopic measurements performed on dust particles [Grousset *et al.*, 1992]. Discrepancies between the predicted and actual source regions might therefore cause the model's inability to simulate a strong increase in dust deposits during the LGM.

7.2. Transport of Dust Toward Greenland

*Comparison with paleoclimatic data.* Over Greenland, the simulated annual mean dust concentration in snow (total removal flux of dust over snow accumulation) increases by a factor of 4 during the LGM. This increase is stronger than over Antarctica, but it is still below the level of the changes observed in ice cores. Indeed, at Camp Century, in northwest Greenland, the observed increase reaches a factor of 100 [Thompson, 1977a] and in Dye 3, south of Greenland, a factor of 70 [Hammer *et al.*, 1985]. Similar to results from Antarctica, the model results are too low by a factor of 10 to 20. However, we compare the simulated results to the maximum dust increase observed during the glacial maximum, but ice cores exhibit quite a high variability all along this period. For example, at Dye 3, the observed increase varies from a factor of 3 to 70 during the glacial period [Hammer *et al.*, 1985]. The model-data discrepancy might therefore be less than stated here.

*Atmospheric patterns and origin of dust deposits.* For the present-day climate, the strongest simulated transport of dust occurs over the North Atlantic in February and mainly comes from the Saharan source (Figure 17 and Table 5). In August, the transport of dust is strongest from Arabia-Asia, although less efficient than in February. The resulting seasonal contrast corresponds to twice as much dust in February as in August for

the present-day climate (Table 5). This result is in good agreement with observations at Camp Century which show a maximum of dust deposition in winter and early spring with a maximum over minimum ratio of 2 to 3 [Thompson, 1977a].

During the LGM, the seasonal contrast is reversed. The transport of dust is more important in August with an increase in the dust concentration in snow by a factor of 10 during this season (Table 5). On annual average, this increase is, however, weakened by the smaller increase during the winter season. In August, the increase in the dust concentration in snow corresponds to an increase in the atmospheric dust content by a factor of 2 to 5 north of Europe (Figure 16). The latter was mentioned previously and was seen to result from the cyclonic circulation located north of Europe during the August LGM climate (Figure 6) which favors a transport from both the Saharan and Arabian-Asian sources (Table 5). In the February LGM climate, the global contribution from the Sahara is weakened since the northward transport which occurs over the North Atlantic during the present-day climate vanishes. During this season the transport of dust from Arabia-Asia and from the Sahara takes place through the cyclonic circulation developing over Europe (Figure 5). The change of circulation and the reduced precipitation amount lead to a strong decrease in the intensity of the dust removal flux, although the dust concentration in snow is increased, especially in the southern latitudes.

*Discussion.* Similar to the discrepancy for Antarctica, the model-data discrepancy for Greenland can result from model deficiencies, such as biases in the circulation patterns and/or in the dust modeling. For example, the model overestimates the reduced snow accumulation in southern Greenland (section 4.2). The transport of Saharan dust in the February present-day climate might also be overestimated as a result of the strong transient northward transport occurring over the North Atlantic during the 60-day mean [Joussaume, 1990]. However, it is doubtful that the increase would exceed the factor of 10 simulated in the summer season, which is still underestimated by an order of magnitude. Therefore, as for the southern hemisphere, it is likely that the model underestimates the source areas for the LGM. Because the simulated Saharan and

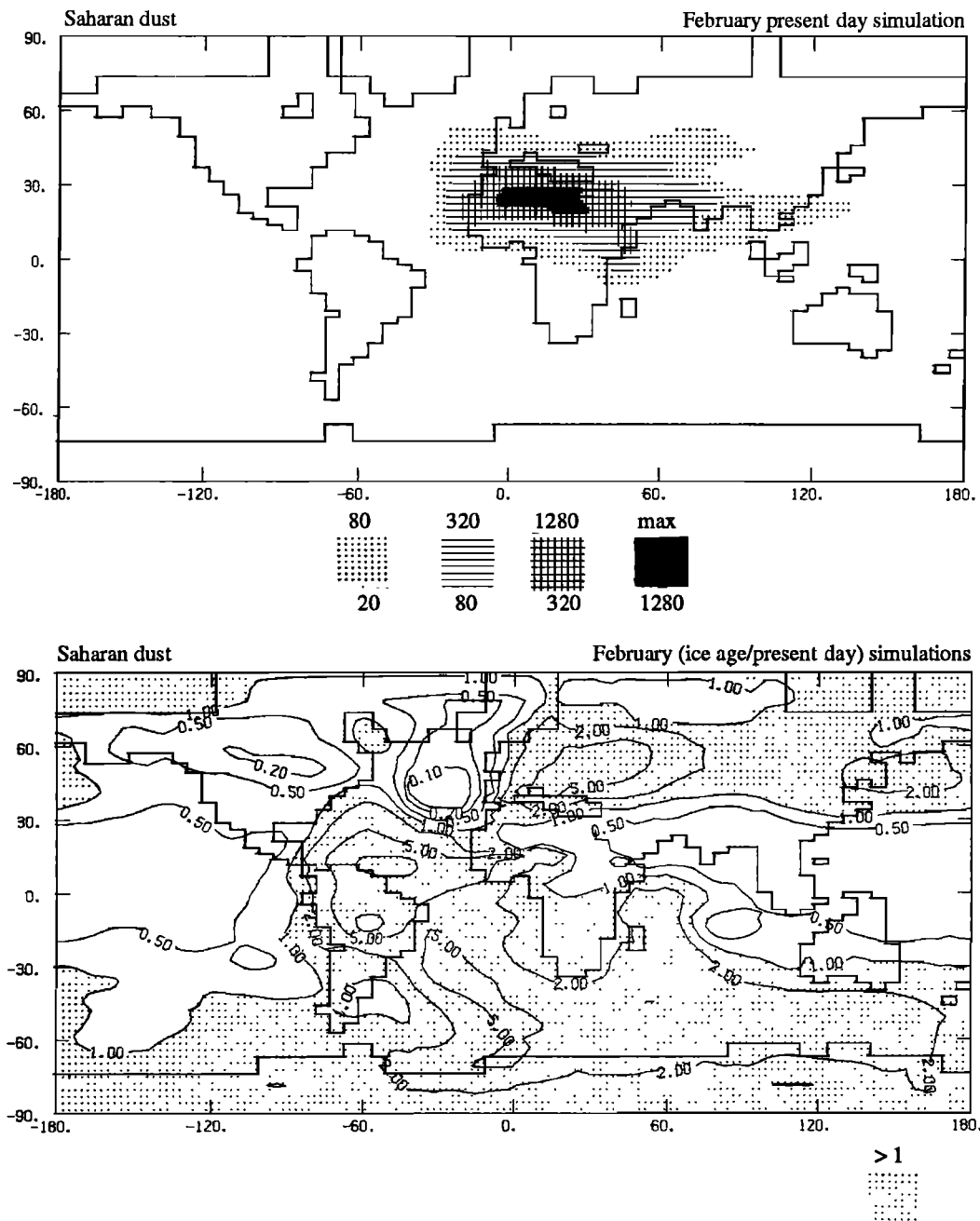


Fig. 17. Simulated transport of dust originating from the Sahara (including the Horn of Africa and southern Europe) for February. Vertically integrated mass of dust: (top) present day, where shaded areas are 20, 80, 320 and 1280  $\text{kgAU m}^{-2}$ ; (middle) ice age over present day ratio, where the ratio is filtered as in Figure 4 with isolines 1/10, 1/5, 1/2, 1, 2, 5 and 10, and dotted areas for values above 1; (bottom) vertically integrated dust fluxes for the ice age simulation ( $\text{kgAU m}^{-1} \text{s}^{-1}$ ). Isolines are at every  $5 \times 10^3 \text{ kgAU m}^{-1} \text{s}^{-1}$ . Hatched areas represent source regions. Northward, westward, southward and eastward fluxes ( $10^8 \text{ kgAU m}^{-1} \text{s}^{-1}$ ) from the indicated box are computed for the dust transport by the total, mean and transient flows, the two latter being in parentheses. The present day dust fluxes can be found in the work of Joussaume [1990].

Arabian-Asian deserts reach an important extent during the LGM, the underestimation might come from the occurrence of other source areas which would not be predicted by the model. This assessment is supported by Hammer *et al.* [1985] who suggest that the ocean free continental shelves could have been a potential source of dust, in agreement with the high alkalinity of the dust during the LGM. The sources of loess deposits (particles in the 5- to 50- $\mu\text{m}$  range) in Europe and Asia could also have been potential sources of windblown terrestrial material [Hammer *et al.*, 1985]. The latter might

have resulted from the outwash by meltwater from glaciers [Flint, 1971] and been favored by freezing and dry conditions. However, it is not yet proved that the sources of loess indeed made enough fine particles available for long-range transport. Moreover, even the time scale might differ since Wintle *et al.* [1984] date the formation of loess for western Europe around 12 kyr B.P. to 16 kyr B.P., thus after the major dust increase in Greenland.

Nevertheless, the simulated results tend to suggest that sources located in northern Europe and/or northern Asia could

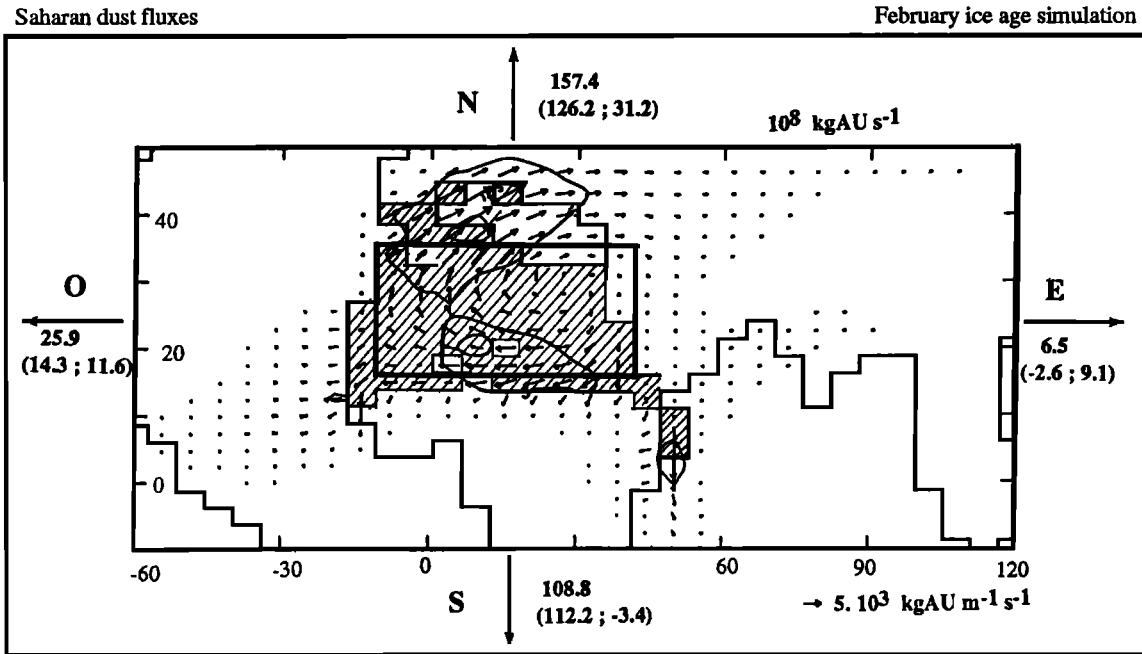


Fig. 17. (continued)

have been very favorable to a dust transport toward Greenland, especially in August. This result is in good agreement with the suggestion made by *Hammer et al.* [1985] that the continental shelves of the northern USSR could have been an important dust source. Thanks to the proximity of these areas with Greenland and to the favorable transport paths, even small extended sources could have been very efficient. Conversely, in the model, the transport of dust from western North America is inhibited by the sea ice expansion which prevents the northward transport over the North Atlantic.

### 7.3. Comparison With Paleoclimatic Data From Marine Sediments

Aeolian transport of continental dust can be the prevailing source of mineral particles found in marine sediments, especially far from the continent [*Blank et al.*, 1985]. For example, the quartz content of marine sediments reproduces the main transport patterns of continental dust for the present-day climate [*Leinen et al.*, 1986]. For the LGM, analyses of the changes in the quartz content have been performed for some areas and can be used to test the model results over oceanic areas, although the quartz content corresponds to slightly bigger particles (5 to 10  $\mu\text{m}$ ) and may bias the comparison.

Over the tropical Atlantic Ocean, *Kolla et al.* [1979] show an equatorward expansion of the quartz rich marine sediments along the west African coast, with an increase in the quartz content of the order of 2 to 6 at 0°-15°N for the LGM. The analyses of the terrigenous silt content in the same area by *Sarnthein and Koopman* [1980] also show an equatorward expansion of the plume but no displacement of the maximum. They observe twice as much dust flux into the ocean in the ice age. The simulated results agree with an increased dust transport over the tropical Atlantic Ocean (Figures 17 and 18) and give a net annual mean increase in the dust removal flux of the order of 2 near the equator (Figure 14), which is due to the southward expansion of the Saharan dust source and to stronger trade winds (section 6.3), in agreement with paleoclimatic data

[*Sarnthein*, 1978; *Sarnthein et al.*, 1981]. Further north over the Atlantic Ocean, the quartz content of marine sediments increases during the LGM along the sea ice margin around 45°N [*Kolla et al.*, 1979]. This observed increase could be associated with ice rafting of quartz grains [*Kolla et al.*, 1979], but it could also reflect a stronger transport from the tropics [*Robinson*, 1986], the latter interpretation being supported by our simulated results (Figures 14 and 18).

In the Indian Ocean, *Kolla and Biscaye* [1977] observe an increase in the quartz accumulation by a factor of 2, south of the Arabian Sea and northwest of Australia, in good agreement with the simulated results (Figure 14). The simulated changes result from a stronger southward transport from Arabia and the Horn of Africa in February (Figures 15 and 5) and from stronger trade winds off the western Australian coast in August (Figures 16 and 6). Over these areas, the increase in the dust removal fluxes is not related to any increase in the atmospheric dust content. This last feature warns against an excessive interpretation of dust deposit changes directly in terms of changes in the atmospheric dust content.

In the Pacific Ocean, the transport of dust from Asia toward the North Pacific is weakly modified during the LGM according to marine sediments [*Leinen*, 1989]. It even decreases around 40°N in the central Pacific [*Rea et al.*, 1985]. The simulated results are in fairly good agreement with these observations, although a slight increase is simulated north of 30°N (Figure 14). The latter feature results from the stronger Aleutian Low in August, which is the prevailing season of dust transport in the present-day simulations, in disagreement with observations [*Joussaume*, 1990]. In the eastern equatorial Pacific, the quartz content decreases during the LGM in both paleoclimatic data [*Rea et al.*, 1985] and model results (Figure 14). This simulated result supports the interpretation suggested by *Rea et al.* [1985], who explain the change in the dust transport as resulting from changes in the source regions.

## 8. CONCLUSIONS

A global cooling of 3.6°C and a slightly weaker intensity

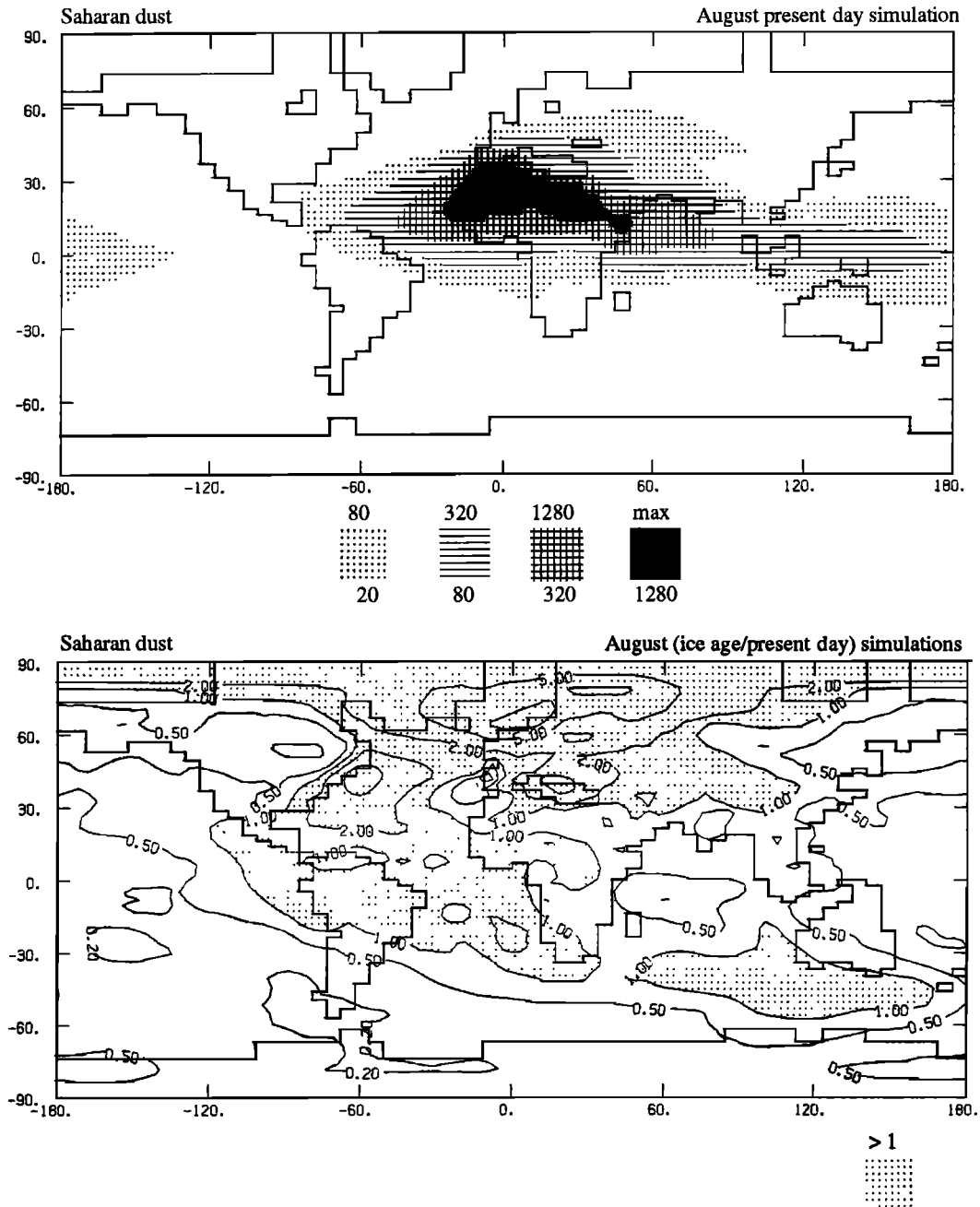


Fig. 18. Same as Figure 17 but for August.

of the hydrological cycle are simulated for the ice age climate by the LMD AGCM. The changes are, however, far from being uniform over the globe. The most important cooling occurs in the northern hemisphere extratropical latitudes where it is associated with important changes in the atmospheric circulation. Consistent with the increased meridional temperature gradient, stronger westerly winds are simulated, especially over Europe. The planetary wave structure of the mean circulation is also strengthened in both summer and winter seasons, and allows an enhanced poleward transport of energy. In the winter season, an anticyclonic circulation takes place over the elevated and cold Laurentide ice sheet leading to a splitting of the jet stream. The cyclonic activity is also strongly affected: weakened over the North Atlantic, where storm tracks remain confined to the southern margin of the sea

ice cover, it is enhanced over the Pacific and expands eastward over the Pacific and Europe. In the tropical regions, convective activity preferentially takes place over the oceanic regions which experience a relative surface warming during the ice age and the summer monsoon is weakened over Asia.

To test the reliability of the reconstructed ice age circulation, we have compared our simulated results to the available estimates derived from various paleoclimatic data. The simulated results are in general agreement with these estimates with, however, two main exceptions. The cooling experienced by the tropical continental areas, southeastern Europe and the Middle East is too weak in our simulations. Concerning the tropical continental regions, our results are consistent with the results obtained by other AGCMs using the same set of boundary conditions, and might result from the

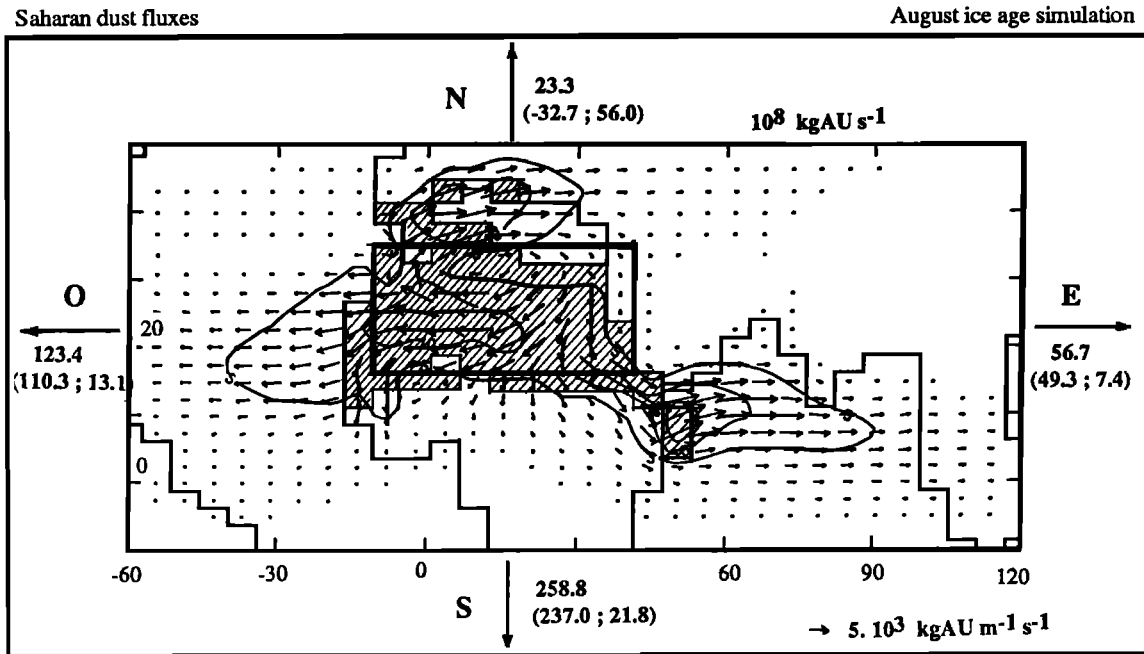


Fig. 18. (continued)

relatively weak surface cooling prescribed over the tropical oceans by the CLIMAP [1981] data set as was emphasized by Rind and Peteet [1985]; if the relatively warmer tropical surface waters had indeed to be questioned, an important limitation of the simulated ice age atmospheric circulation would be stated. Concerning southeastern Europe and the Middle East, the model-data discrepancy is more unique to our AGCM and results from a strong high pressure developing over the eastern Mediterranean Sea during the ice age February climate. The origin of this difference with the other AGCM simulations is not clear. Nevertheless, it is noteworthy that no agreement is obtained between the simulated reconstructions of the European ice age climate obtained by the various AGCMs. More model-model and model-data comparisons would therefore be required to solve this problem and better test the models.

Concerning the desert dust cycle during the ice age climate, the model simulates only a weak global change. The changes are, however, more important at a regional scale where the increase in the atmospheric dust content can reach at least a factor of 2, e.g., over Europe. Nevertheless, the model does not produce any of the great increases in the atmospheric dust content over the high latitudes which are expected from ice core paleoclimatic data. Over East Antarctica, no change is simulated in the dust concentration in snow, compared to an observed 10 to 20 times increase. In Greenland, the simulated increase in the dust concentration in snow reaches a factor of 4 which is still less than the factor of 100 observed at Camp Century.

Many processes can induce this major discrepancy. First, model deficiencies in the simulated present-day and ice age circulations can be involved. For example, the August transport of Australian dust toward Antarctica is strongly dependent on the intensity of the cyclonic activity located south of Australia which is overestimated for the present-day climate. Another example is the transport of Saharan dust in February LGM which is strongly related to the strong high

pressure developing over the eastern Mediterranean Sea, apparently contradicted by paleoclimatic data of temperature change. Other biases can be associated with systematic errors of AGCMs, e.g., AGCMs are not very good at reproducing the climate of the high latitudes, as was reviewed by Schlesinger [1984]. This is the case for the LMD model which overestimates the surface temperature and snow accumulation over Antarctica (part 2).

The other possible causes of the model deficiencies in the dust cycle can be associated with the desert dust modeling itself. Indeed, our modeling is only a first approach and is oversimplified in many respects. The review of the critical points of our dust modeling was fully discussed by Jousaume [1990]. The most important features are the dust mobilization dependency on the wind speed, the dry and wet removal parameterizations, and the too diffusive numerical scheme used for dust advection.

Another source of uncertainty is the atmospheric variability which is insufficiently captured by the averages over 60 days presented here. This feature was repeatedly invoked in the text and must be kept in mind. Moreover, the annual mean has been estimated from the winter and summer seasons only and we might miss an important transport occurring during the intermediate seasons; e.g., the present-day transport of Asian dust toward the North Pacific essentially takes place during the spring [Duce et al., 1980].

Therefore, many uncertainties remain concerning the causes of the weak model performance in simulating the high-latitude changes in the dust cycle observed in ice cores. Nevertheless, it is doubtful that the above mentioned deficiencies can totally explain the strong model-data discrepancies in high latitudes. Indeed, the strongest LGM/present-day local increases reach a factor of 2 over Antarctica and 10 over Greenland, which is still an order of magnitude below the observed changes. The main cause of this model-data discrepancy may therefore result from the most critical point in our dust modeling, i.e., the definition of the source regions. First, we have chosen to

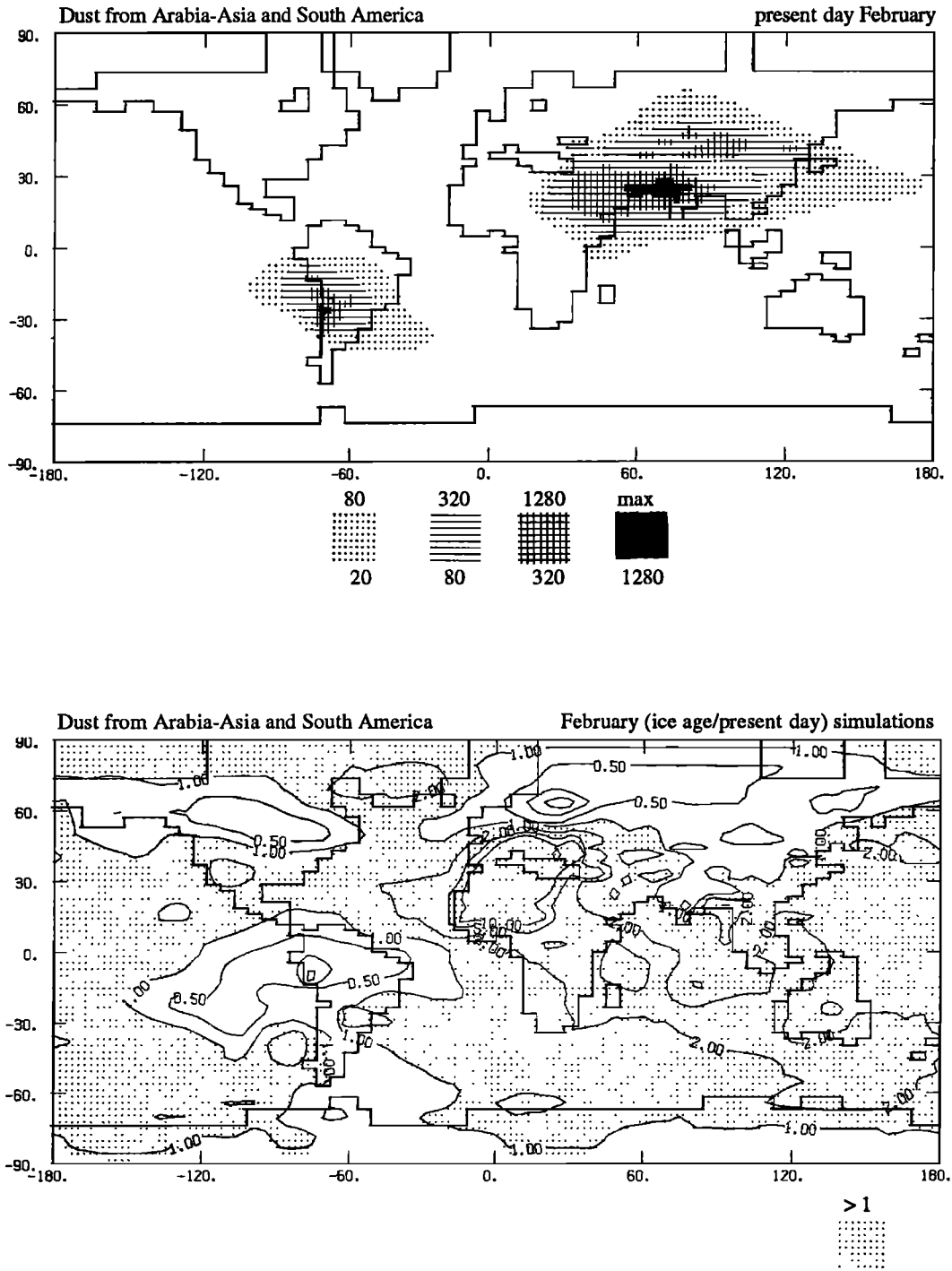


Fig. 19. Simulated transport of dust originating from Arabia-Asia and South America for February. Vertically integrated mass of dust: (top) present day, where shaded areas are 20, 80, 320 and 1280 kgAU m<sup>-2</sup>; (bottom) ice age over present day ratio, where the ratio is filtered as in Figure 4 with isolines 1/10, 1/5, 1/2, 1, 2, 5 and 10, and dotted areas for values above 1

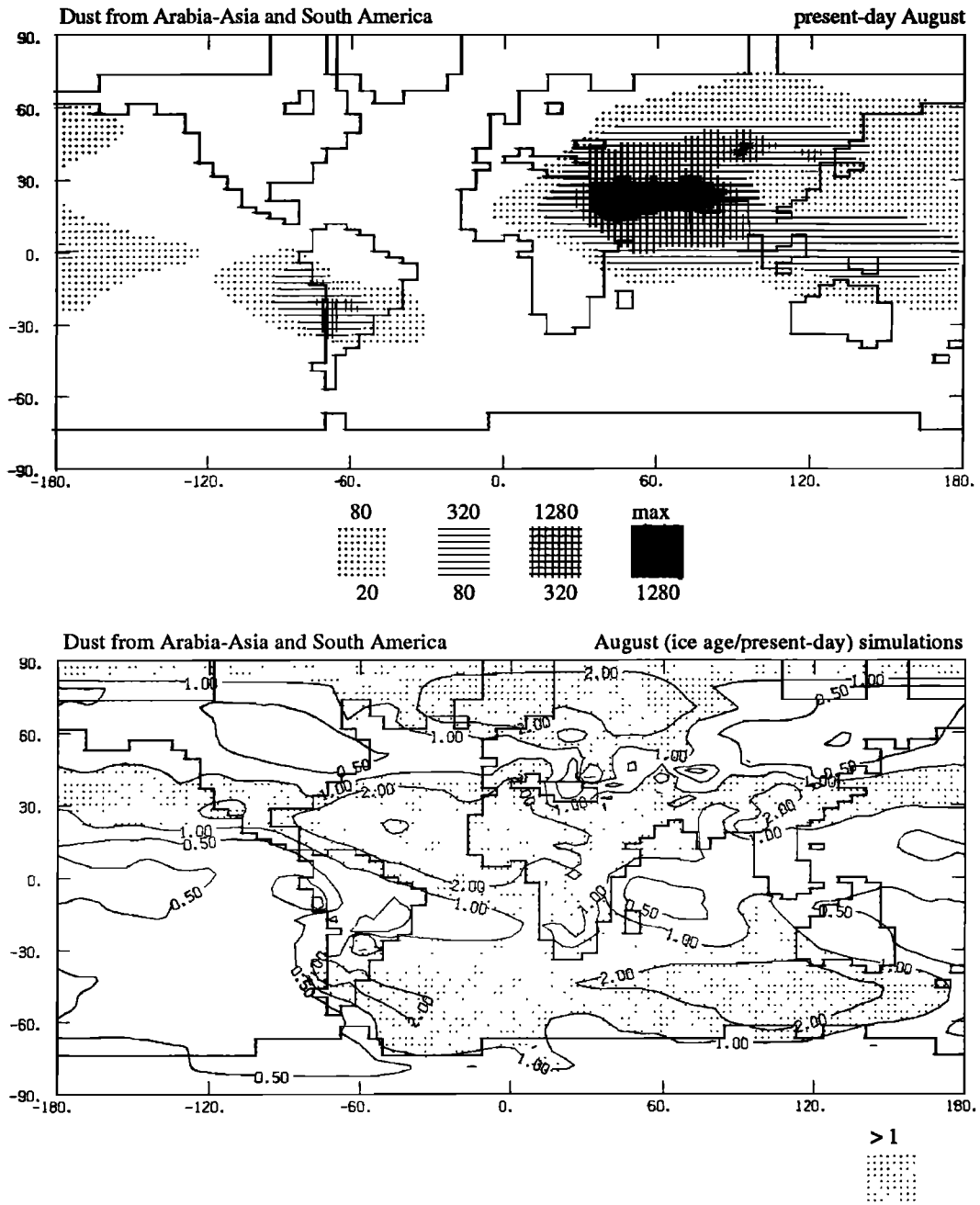


Fig. 20. Same as Figure 19 but for August.

TABLE 4. Global Dust Budgets Over Antarctica

	February		August		Annual mean		Ice Age Over Present
	Present	Ice Age	Present	Ice Age	Present	Ice Age	
<i>East Antarctica: Latitude of 70°03'S, 7 Grid Point Average Between 95°37'E and 135°E</i>							
Precipitation, mm d <sup>-1</sup>	0.73	0.24	0.97	0.39	0.85	0.32	0.38
Wet removal flux, 10 <sup>-3</sup> kgAU m <sup>-2</sup> d <sup>-1</sup>	183	150	1475	468	829	309	0.37
Sahara	0%	1%	2%	5%	2%	4%	0.64
South Africa	16%	7%	3%	7%	4%	7%	0.81
South America	19%	30%	3%	11%	5%	16%	1.28
Australia	65%	62%	92%	77%	89%	73%	0.31
Dry removal flux, 10 <sup>-3</sup> kgAU m <sup>-2</sup> d <sup>-1</sup>	77	53	239	113	158	83	0.53
Total removal flux, 10 <sup>-3</sup> kgAU m <sup>-2</sup> d <sup>-1</sup>	260	203	1714	581	987	392	0.40
Dust concentration in snow (total removal flux /precipitation)	0.36	0.83	1.77	1.50	1.16	1.23	1.06
<i>East Antarctica: Latitude of 78°31'S, 7 Grid Point Average Between 95°37'E and 135°E</i>							
Precipitation, mm d <sup>-1</sup>	0.25	0.21	0.30	0.07	0.28	0.14	0.50
Wet removal flux, 10 <sup>-3</sup> kgAU m <sup>-2</sup> d <sup>-1</sup>	28	33	183	65	105	49	0.47
Sahara	1%	1%	5%	3%	5%	3%	0.24
South Africa	17%	6%	7%	5%	8%	5%	0.28
South America	46%	39%	8%	8%	13%	18%	0.67
Australia	36%	54%	80%	84%	74%	74%	0.47
Dry removal flux, 10 <sup>-3</sup> kgAU m <sup>-2</sup> d <sup>-1</sup>	20	16	47	13	34	15	0.44
Total removal flux, 10 <sup>-3</sup> kgAU m <sup>-2</sup> d <sup>-1</sup>	48	49	230	78	139	64	0.46
Dust concentration in snow (total removal flux /precipitation)	0.19	0.23	0.77	1.11	0.50	0.46	0.92
<i>West Antarctica: Latitude of 78°31'S, 5 Grid Point Average Between 106°53'W and 135°W</i>							
Precipitation, mm d <sup>-1</sup>	0.99	1.64	1.13	1.58	1.06	1.61	1.52
Wet removal flux, 10 <sup>-3</sup> kgAU m <sup>-2</sup> d <sup>-1</sup>	111	441	413	720	262	580	2.22
Sahara	0%	1%	14%	4%	11%	3%	0.56
South Africa	6%	3%	5%	4%	5%	3%	1.51
South America	16%	11%	18%	8%	18%	9%	1.18
Australia	78%	85%	63%	84%	66%	85%	2.83
Dry removal flux, 10 <sup>-3</sup> kgAU m <sup>-2</sup> d <sup>-1</sup>	20	44	25	51	22	48	2.13
Total removal flux, 10 <sup>-3</sup> kgAU m <sup>-2</sup> d <sup>-1</sup>	131	485	438	771	284	628	2.21
Dust concentration in snow (total removal flux /precipitation)	0.13	0.30	0.39	0.49	0.27	0.39	1.44
<i>Global Average Over the Grid Points Covering the Antarctica Continent</i>							
Precipitation, mm d <sup>-1</sup>	0.72	0.66	0.70	0.51	0.71	0.59	0.83
Wet removal flux, 10 <sup>-3</sup> kgAU m <sup>-2</sup> d <sup>-1</sup>	124	239	448	333	286	286	1.00
Sahara	1%	1%	6%	4%	5%	3%	0.53
South Africa	16%	6%	10%	4%	11%	5%	0.40
South America	48%	42%	12%	18%	20%	28%	1.41
Australia	35%	51%	72%	74%	64%	64%	1.02
Dry removal flux, 10 <sup>-3</sup> kgAU m <sup>-2</sup> d <sup>-1</sup>	37	51	62	46	50	49	0.98
Total removal flux, 10 <sup>-3</sup> kgAU m <sup>-2</sup> d <sup>-1</sup>	161	290	510	379	336	335	1.00
Dust concentration in snow (total removal flux /precipitation)	0.22	0.44	0.73	0.74	0.47	0.57	1.20

predict the source regions by the model itself. Although very satisfactory, this approach is probably too optimistic with regard to the AGCMs' ability to reproduce the ground hydrology. Moreover, defining the source regions is a difficult problem. For example, all the desertic areas are not efficient sources of fine dust, especially the core deserts which are poor sources [Joussaume, 1990]. Thus, by considering all the desertic areas as sources of dust, we probably underestimate the changes occurring during the glacial period. Second, the desert dust amount transported toward high latitudes is very sensitive to the distance to the source. Very small extended areas located nearer to the poles could be very efficient sources. To go beyond the present study, we would need to test several assumptions of potential source regions during the LGM, for example, the ocean free continental ice shelves and/or the

source regions for loess.

Nevertheless, even if we cannot yet explain the great increase in the dust content found in ice cores for the ice age, the present study is a first step toward a new kind of modeling approach that can be used to help the interpretation of paleoclimatic data. Another example is also presented in part 2 of the present paper and concerns the water isotopes. Concerning our modeling of the desert dust cycle, it is crude in many respects and could be improved in the future, although a more exhaustive knowledge of the present-day climatology of the dust transport should be available to better validate the desert dust model [Joussaume, 1990]. For the ice age, the definition of the source regions is probably the most critical problem and would require sensitivity experiments to various assumptions of the localization of the dust sources.

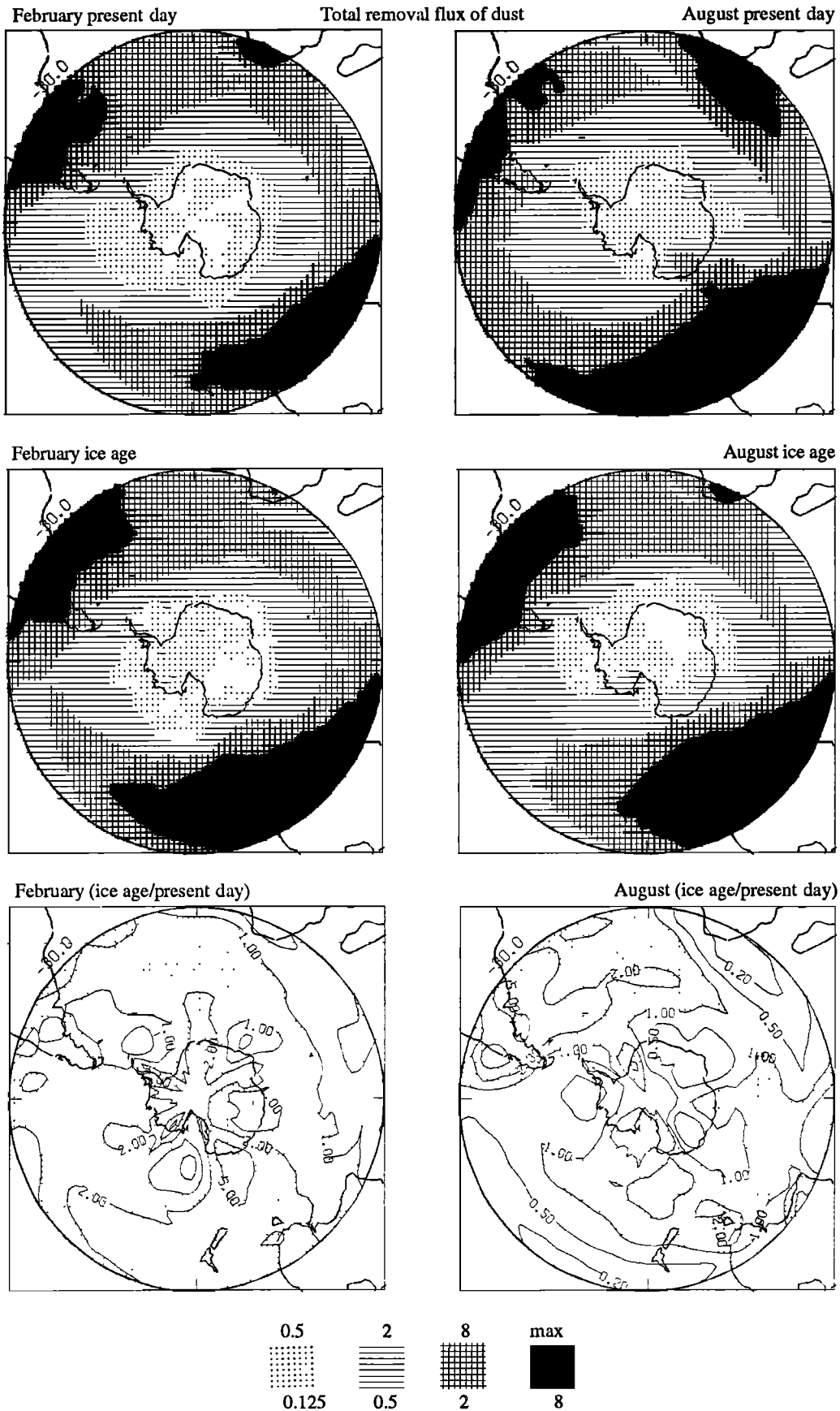


Fig. 21. Total removal flux of dust above Antarctica simulated for the (top) present-day and (middle) ice age (left) February and (right) August simulations. Shaded areas are in a geometrical progression of ratio 4: 0.125, 0.5, 2, 8 kgAU m<sup>-2</sup> d<sup>-1</sup>. (Bottom) Ice age over present day ratios of the total removal flux of dust. The field has been filtered as in Figure 4 and is displayed with isolines 1/10, 1/5, 1/2, 1, 2, 5 and 10, and dotted areas for values above 1.

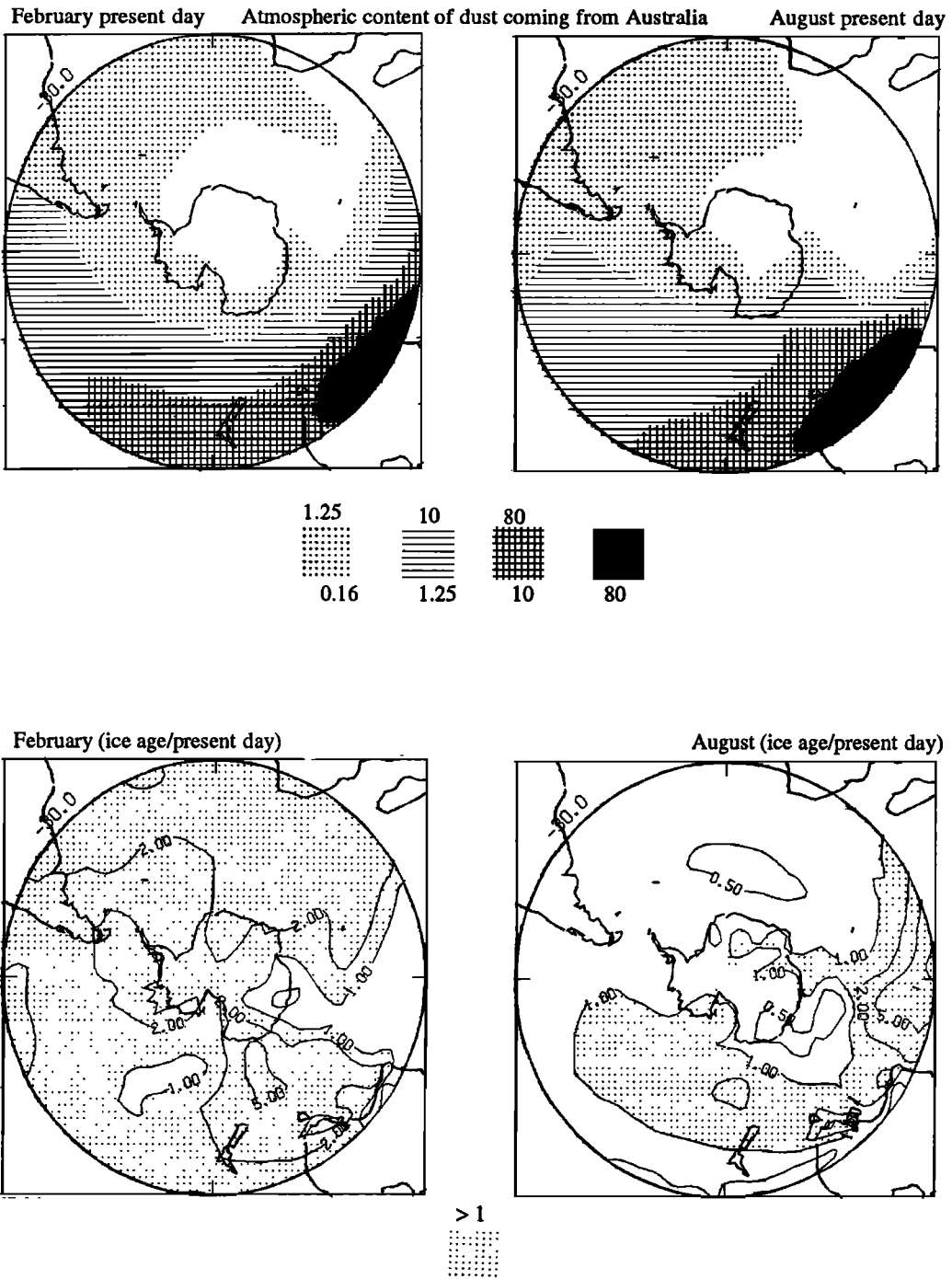


Fig. 22. Simulated transport of dust originating from Australia. Vertically integrated mass of dust for (left) February and (right) August simulations: (top) present day, where shaded areas are 0.16, 1.25, 10 and 80 kgAU m<sup>-2</sup>; (bottom) ice age over present day ratio, where the ratio is filtered as in Figure 4 with isolines 1/10, 1/5, 1/2, 1, 2, 5 and 10, and dotted areas for values above 1.

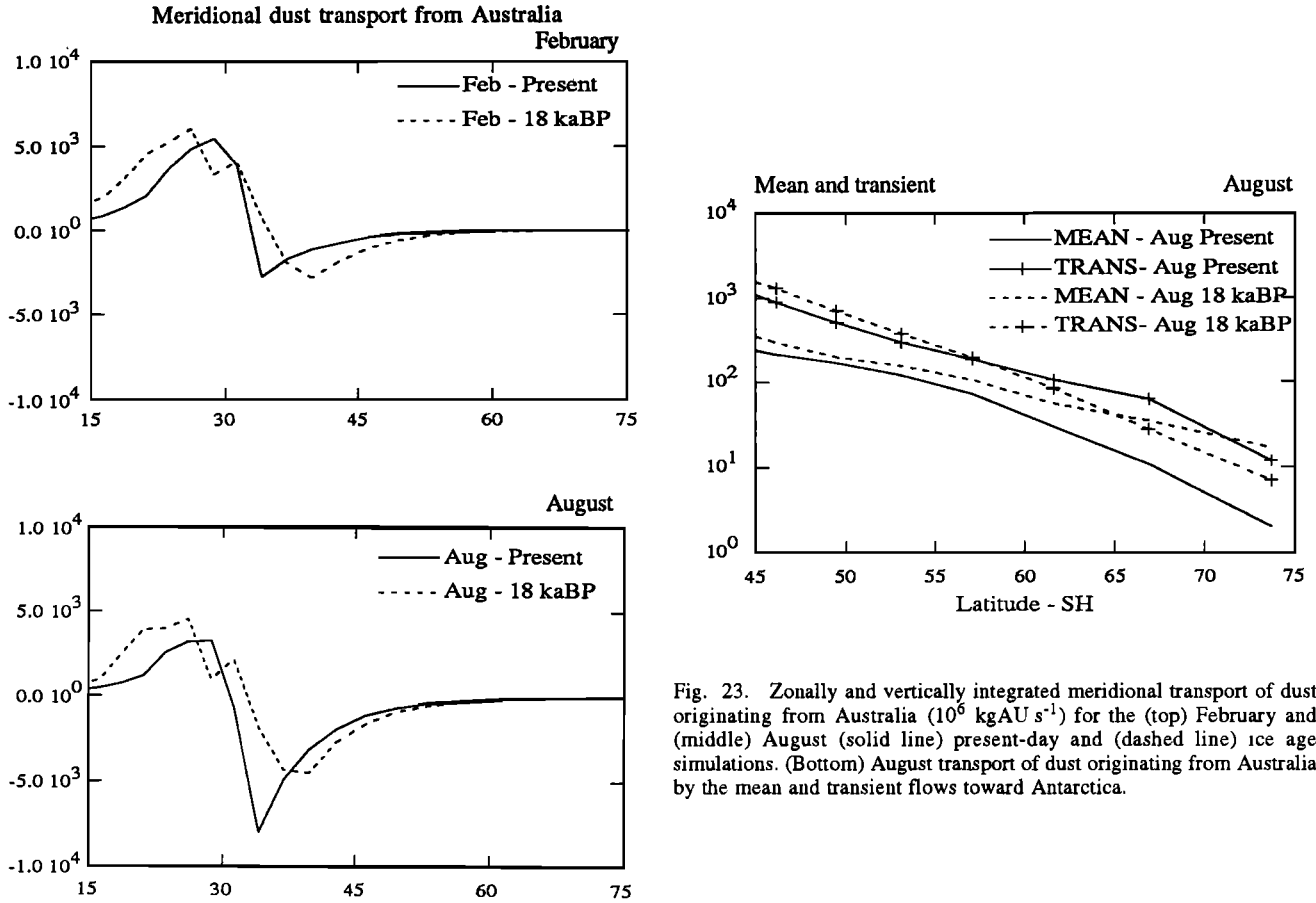


Fig. 23. Zonally and vertically integrated meridional transport of dust originating from Australia ( $10^6$  kgAU  $s^{-1}$ ) for the (top) February and (middle) August (solid line) present-day and (dashed line) ice age simulations. (Bottom) August transport of dust originating from Australia by the mean and transient flows toward Antarctica.

TABLE 5 Global Dust Budgets over Greenland

	February		August		Annual mean		Ice Age Over Present
	Present	Ice Age	Present	Ice Age	Present	Ice Age	
<i>Northern Greenland: Latitude of 78°31'N, 5 Grid Point Average</i>							
Precipitation, mm d <sup>-1</sup>	0.95	0.96	0.97	0.64	0.96	0.80	0.83
Wet removal flux, 10 <sup>-3</sup> kgAU m <sup>-2</sup> d <sup>-1</sup>	358	645	120	891	239	768	3.21
Sahara	79%	39%	32%	30%	67%	34%	1.62
Arabia-Asia	12%	58%	62%	70%	25%	65%	8.48
North America	9%	3%	6%	0%	8%	1%	0.54
Dry removal flux, 10 <sup>-3</sup> kgAU m <sup>-2</sup> d <sup>-1</sup>	107	49	97	628	102	339	3.32
Total removal flux, 10 <sup>-3</sup> kgAU m <sup>-2</sup> d <sup>-1</sup>	465	694	217	1519	341	1107	3.20
Dust concentration in snow (Total removal flux /precipitation)	0.50	0.72	0.22	2.37	0.36	1.38	3.90
<i>Southern Greenland: Latitudes of 70°03'N and 64°10'N, 6 (7) Grid Point Average For the Present Day (Ice Age)</i>							
Precipitation, mm d <sup>-1</sup>	4.14	0.29	5.88	0.66	5.01	0.48	0.10
Wet removal flux, 10 <sup>-3</sup> kgAU m <sup>-2</sup> d <sup>-1</sup>	1346	132	1059	870	1202	501	0.42
Sahara	68%	29%	32%	61%	52%	56%	0.45
Arabia-Asia	13%	55%	60%	38%	34%	41%	0.50
North America	19%	16%	8%	1%	14%	3%	0.09
Dry removal flux, 10 <sup>-3</sup> kgAU m <sup>-2</sup> d <sup>-1</sup>	179	67	146	185	162	126	0.77
Total removal flux, 10 <sup>-3</sup> kgAU m <sup>-2</sup> d <sup>-1</sup>	1524	199	1205	1054	1365	627	0.46
Dust concentration in snow (Total removal flux /precipitation)	0.37	0.69	0.20	1.60	0.27	1.31	4.85

**Acknowledgments.** I thank R. Sadourny for his important contribution in the development of the dust modeling inside the LMD AGCM. I also thank J. Portes and G. Rabreau for their help in the development of graphics. This project was supported by the Programme National d'Etude de la Dynamique du Climat. The computing time was provided by the Centre de Calcul Vectoriel pour la Recherche. I particularly thank C. Genthon, T. Webb, M. Lautenschlager and the anonymous referees for their very useful comments on the text.

## REFERENCES

- Bard, E., B. Hamelin, R. G. Fairbanks, and A. Zindler, Calibration of the  $^{14}\text{C}$  timescale over the past 30,000 years using mass spectrometric U-Th ages from Barbados corals, *Nature*, **345**, 405-409, 1990.
- Barnola, J. M., D. Raynaud, Y. S. Korotkevitch, and C. Lorius, Vostok ice core: A 160,000 year record of atmospheric  $\text{CO}_2$ , *Nature*, **329**, 408-414, 1987.
- Bartman, F. L., A time variable model of earth's albedo, *NASA Contract Rep.*, 159259, 159-259, 1980.
- Beer, J., H. Oeschger, M. Andrée, G. Bonani, M. Suter, W. Wölfli, and C. C. Langway, Jr., Temporal variations in the  $^{10}\text{Be}$  concentration levels found in the Dye 3 ice core, Greenland, *Ann. Glaciol.*, **5**, 16-17, 1984.
- Berger, A., Long-term variations of caloric solar radiation resulting from the earth's orbital elements, *Quat. Res.*, **9**, 139-167, 1978.
- Blank, M., M. Leinen, and J. M. Prospero, Major Asian aeolian inputs indicated by the mineralogy of aerosols and sediments in the western North Pacific, *Nature*, **314**, 84-86, 1985.
- Bonnefille, R., and G. Riollet, The Kashiru pollen sequence (Burundi) palaeoclimatic implications for the last 40,000 yr BP in tropical Africa, *Quat. Res.*, **30**, 19-35, 1988.
- Bonnefille, R., J. C. Roeland, and J. Guiot, Temperature and rainfall estimates for the past 40,000 years in equatorial Africa, *Nature*, **346**, 347-349, 1990.
- Bowler, J. M., Glacial age aeolian events at high and low latitudes: A southern hemisphere perspective, in *Antarctic Glacial History and World Palaeoenvironments*, edited by E. M. van Zinderen Bakker, pp. 149-172, 1977.
- Braine-Bonnaire, T., Etude de la variabilité intrasaisonnière de l'atmosphère tropicale simulée par un modèle de circulation générale, *thèse de doctorat*, 244 pp., Univ. de Paris VI, Paris, 1989.
- Broccoli, A. J., and S. Manabe, The influence of continental ice, atmospheric  $\text{CO}_2$ , and land albedo on the climate of the Last Glacial Maximum climate, *Clim. Dyn.*, **1**, 87-99, 1987.
- Climate: Long Range Investigation, Mapping and Prediction Group, The surface of the ice age earth, *Science*, **191**, 1131-1136, 1976.
- Climate: Long Range Investigation, Mapping and Prediction Group, Seasonal reconstructions of the Earth's surface at the Last Glacial Maximum, *Geol. Soc. Am., Map Chart Ser. MC-36*, Boulder, Colo., 1981.
- Cook, K. H., and I. M. Held, Stationary waves of the ice age climate, *J. Clim.*, **1**, 807-819, 1988.
- Dansgaard, W., and H. Oeschger, Past environmental long-term records from the Arctic, in *The Environmental Record in Glaciers and Ice Sheets*, *Phys. Chem. and Earth Sci. Res. Rep.*, vol. 8, edited by H. Oeschger and C. C. Langway Jr., pp. 287-318, J. Wiley, New York, 1989.
- De Angelis, M., N. I. Barkov, and V. N. Petrov, Aerosol concentrations over the last climatic cycle (160 kyr) from an Antarctic ice core, *Nature*, **325**, 318-321, 1987.
- Duce, R. A., C. K. Unni, B. J. Ray, J. M. Prospero, and J. T. Merrill, Long-range atmospheric transport of soil dust from Asia to the tropical North Pacific: Temporal variability, *Science*, **209**, 1522-1524, 1980.
- Duplessy, J. C., Glacial to interglacial contrasts in the northern Indian Ocean, *Nature*, **295**, 494-498, 1982.
- Flint, R. F., *Glaciology and Quaternary Geology*, 892 pp., John Wiley, New York, 1971.
- Gates, W. L., Modeling the ice age climate, *Science*, **191**, 1138-1144, 1976a.
- Gates, W. L., The numerical simulation of ice-age climate with a global general circulation model, *J. Atmos. Sci.*, **33**, 1844-1873, 1976b.
- Gaudichet, A., J. R. Petit, R. Lefèvre, and C. Lorius, An investigation by analytical transmission microscopy of individual microparticles from Antarctic (Dôme C) ice core samples, *Tellus Ser. B*, **38**, 250-261, 1986.
- Gaudichet, A., M. de Angelis, R. Lefèvre, J. R. Petit, Y. S. Korotkevitch, and V. N. Petrov, Mineralogy of insoluble particles in Vostok Antarctic ice core over the last climatic cycle (150 kyr), *Geophys. Res. Lett.*, **15**, 1471-1474, 1988.
- Gaudichet, A., M. de Angelis, S. Joussaume, J. R. Petit, Y. S. Korotkevitch, and V. N. Petrov, Comments on the origin of dust in East Antarctica for present and ice age conditions, *J. Atmos. Chem.*, **14**, 129-142, 1992.
- Gillette, D. A., Environmental factors affecting dust emission by wind erosion, in *Saharan Dust: Mobilization, Transport, Deposition*, edited by C. Morales, *SCOPE Rep.*, **14**, 27-48, 1979.
- Gillette, D. A., J. Adams, A. Endo, and D. Smith, Threshold velocities for input of soil particles in the air by desert soils, *J. Geophys. Res.*, **85**, 5621-5630, 1980.
- Grousset, F. E., P. E. Biscaye, M. Revel, J. R. Petit, K. Pye, S. Joussaume, and J. Jouzel, Antarctic (Dôme C) ice-core dust at 18 ky BP: isotopic constraints on origins, *Earth Planet. Sci. Lett.*, **111**, 175-182, 1992.
- Guiot, J., Methodology of the last climatic cycle reconstruction in France from pollen data, *Palaeogeogr. Palaeoclim. Palaeoecol.*, **80**, 49-69, 1990.
- Hansen, J. E., A. Lacis, D. Rind, G. Russell, P. Stone, I. Fung, R. Ruedy, and J. Lerner, Climate: Analysis of feedback mechanisms, in *Climate Processes and Climate Sensitivity*, *Geophys. Monogr. Ser.*, vol. 29, edited by J. E. Hansen, and T. Takahashi, pp. 130-163, AGU, Washington, D. C., 1984.
- Hammer, C. U., H. B. Clausen, W. Dansgaard, A. Neftel, P. Kristinsdottir, and E. Johnson, Continuous impurity analysis along the Dye 3 deep core, in *Greenland Ice Core: Geophysics, Geochemistry and the Environment*, *Geophys. Monogr. Ser.*, vol. 33, edited by C. C. Langway, Jr., H. Oeschger, and W. Dansgaard, pp. 90-94, AGU, Washington, D. C., 1985.
- Held, I. M., Stationary and quasi-stationary eddies in the extratropical atmosphere: Theory, in *Large-Scale Dynamical Processes in the Atmosphere*, edited by B. J. Hoskins and R. P. Pearce, pp. 127-168, Academic, San Diego, Calif., 1983.
- Joussaume, S., Simulations du climat du dernier maximum glaciaire à l'aide d'un modèle de circulation générale de l'atmosphère incluant une modélisation du cycle des isotopes de l'eau et des poussières d'origine désertique, *thèse de Doctorat d'Etat*, 507 pp., Univ. de Paris VI, Paris, 1989.
- Joussaume, S., Three-dimensional simulations of the atmospheric cycle of desert dust particles using a general circulation model, *J. Geophys. Res.*, **95**, 1909-1941, 1990.
- Joussaume, S., and J. Jouzel, Paleoclimatic tracers: An investigation using an atmospheric general circulation model under ice age conditions, 2, Water isotopes, *J. Geophys. Res.*, this issue.
- Joussaume, S., J. Jouzel, and R. Sadourny, A general circulation model of water isotope cycles in the atmosphere, *Nature*, **311**, 24-29, 1984.
- Jouzel, J., C. Lorius, J. R. Petit, C. Genthon, N. I. Barkov, V. M. Kotlyakov, and V. M. Petrov, Vostok ice core: A continuous isotope temperature record over the last climatic cycle (160,000 years), *Nature*, **329**, 403-408, 1987.
- Kolla, V., and P. E. Biscaye, Distribution and origin of quartz in the sediments of the Indian Ocean, *J. Sediment. Petrol.*, **47**, 642-649, 1977.
- Kolla, V., P. E. Biscaye, and A. F. Hanley, Distribution of quartz in late quaternary Atlantic sediments in relation to climate, *Quat. Res.*, **11**, 261-277, 1979.
- Kutzbach, J. E., and P. J. Guetter, The influence of changing orbital parameters and surface boundary conditions on climate simulations for the past 18,000 years, *J. Atmos. Sci.*, **43**, 1726-1759, 1986.
- Larson, J. C., and B. R. Barkstrom, Effects of realistic angular reflection laws for the earth-atmosphere albedo, in *Proceedings of the Symposium on Radiation in the Atmosphere 19-28 August 1976*, pp. 451-453, Science, New York, 1977.
- Lautenschlager, M., and K. Herterich, Climatic response to ice age conditions, 1; The atmospheric circulation, *Rep. 42*, Max Planck Inst. für Meteorol., Hamburg, Germany, 1989.
- Lautenschlager, M., and K. Herterich, Atmospheric response to ice age conditions --Climatology near the Earth's surface, *J. Geophys. Res.*, **95**, 22,547-22,557, 1990.
- Leinen, M., The late Quaternary record of atmospheric transport to the northwest Pacific from Asia, in *Paleoclimatology and Paleometeorology: Modern and Past Patterns of Global Atmospheric Transport*, *NATO ASI Ser. C*, vol. 282, edited by M. Leinen and M. Sarnthein, pp. 693-732, Kluwer Academic, Boston, Mass., 1989.

- Leinen, M., D. Cwienk, G. R. Heath, P. E. Biscaye, V. Kolla, J. Thiede, and J. P. Dauphin, Distribution of biogenic silica and quartz in recent deep-sea sediments, *Geology*, **14**, 199-203, 1986.
- Le Treut, H., and K. Laval, The importance of cloud-radiation interaction for the simulation of climate, in *New Perspectives in Climate Modelling*, *Dev. Atmos. Sci. Ser.*, vol. 16, edited by A. Berger and C. Nicolis, pp. 199-222, Elsevier, New York, 1984.
- Lorius, C., L. Merlivat, J. Jouzel, and M. Pourchet, A 30,000 yr isotope climatic record from Antarctic ice, *Nature*, **280**, 644-648, 1979.
- Lorius, C., D. Raynaud, J. R. Petit, J. Jouzel, and L. Merlivat, Late glacial maximum-Holocene atmospheric and ice thickness changes from Antarctic ice core studies, *Ann. Glaciol.*, **5**, 88-94, 1984.
- Lorius, C., J. Jouzel, C. Ritz, L. Merlivat, N. I. Barkov, Y. S. Korotkevich, and V. M. Kotlyakov, A 150,000 year climatic record from Antarctic ice, *Nature*, **316**, 591-596, 1985.
- Manabe, S., and A. J. Broccoli, The influence of continental ice sheets on the climate of an ice age, *J. Geophys. Res.*, **90**, 2167-2190, 1985.
- Manabe, S., and D. G. Hahn, Simulation of the tropical climate of an ice age, *J. Geophys. Res.*, **82**, 3889-3911, 1977.
- Michaud, R., Sensibilité de prévisions météorologiques à longue échéance aux anomalies de température superficielle des océans, thèse de Doctorat d'Etat, 145 pp., Univ. of Paris VI, Paris, 1987.
- Michaud, R., Extended memory of the initial conditions in long-range forecast of the January 1983 atmospheric circulation, *J. Clim.*, **3**, 461-482, 1990.
- Oort, A. H., Global atmospheric circulation statistics 1958-1973, *Prof. Pap.*, **14**, 180 pp., Natl. Oceanic and Atmos. Admin., Boulder, Colo., 1983.
- Peterson, G. M., T. Webb III, J. E. Kutzbach, T. Van Der Hammen, T. A. Wijnstra, and F. A. Street, The continental record and environmental conditions of 18,000 yr BP: an initial evaluation, *Quat. Res.*, **12**, 47-82, 1979.
- Petit, J. R., M. Briat, and A. Royer, Ice age aerosol content from East Antarctic ice core samples and past wind strength, *Nature*, **293**, 391-394, 1981.
- Rea, D. K., M. Leinen, and T. Janecek, Geologic approach to the long-term history of atmospheric circulation, *Science*, **227**, 721-725, 1985.
- Rind, D., Components of the ice age circulation, *J. Geophys. Res.*, **92**, 4241-4281, 1987.
- Rind, D., and D. Peteet, Terrestrial conditions at the Last Glacial Maximum and CLIMAP sea-surface temperature estimates: are they consistent, *Quat. Res.*, **24**, 1-22, 1985.
- Robinson, S. G., The late Pleistocene paleoclimatic record of North Atlantic deep-sea sediments revealed by mineral magnetic measurements, *Phys. Earth Planet. Inter.*, **42**, 22-47, 1986.
- Rognon, P., Une extension des déserts (Sahara et Moyen-Orient) au cours du Tardiglaciaire (18 000-10 000 ans BP), *Rev. Geol. Geogr. Phys.*, **22**, 313-328, 1980.
- Sadourny, R. and K. Laval, January and July performance of the LMD general circulation model, in *New Perspectives in Climate Modelling*, *Dev. Atmos. Sci. Ser.*, vol. 16, edited by A. Berger and C. Nicolis, pp. 173-198, Elsevier, New York, 1984.
- Sarnthein, M., Sand deserts during glacial maximum and climatic optimum, *Nature*, **272**, 173-198, 1978.
- Sarnthein, M. and B. Koopman, Late Quaternary deep-sea record on northwest African dust supply and wind circulation, *Paleocol. Afr.*, **12**, 239-253, 1980.
- Sarnthein, M., G. Tetzlaff, B. Koopmann, K. Wolter, and U. Pflaumann, Glacial and interglacial wind regimes over the eastern subtropical Atlantic and north-west Africa, *Nature*, **293**, 193-196, 1981.
- Schlesinger, M. E., Atmospheric general circulation model simulations of the modern Antarctic climate, in *Environment of West Antarctica: Potential CO<sub>2</sub>-Induced Climate*, pp. 151-196, Committee on Glaciology, Polar Research Board, National Research Council, National Academy Press, Washington, D.C., 1984.
- Slinn, W. G. N., Air-to-sea transfer of particles, in *Air-Sea Exchange of Gases and Particles*, edited by P. S. Liss and W. G. N. Slinn, pp. 299-405, D. Reidel, Norwell, Mass., 1983.
- Street-Perrot, F. A., and S. P. Harrison, Lake-levels and climate reconstruction, in *Paleoclimate Analysis and Modeling*, edited by A. D. Hecht, pp. 291-340, John Wiley, New York, 1985.
- Thompson, L. G., Variations in microparticle concentration, size distribution and elemental composition found in Camp Century, Greenland, and Byrd Station, Antarctica, deep ice cores, in *Isotopes and Impurities in Snow and Ice*, *IAHS AISH Publ.*, **118**, 351-364, 1977a.
- Thompson, L. G., Microparticles, ice-sheets and climate, *Rep.*, **64**, 148 pp., Inst. of Polar Stud., Ohio State Univ., Columbus, 1977b.
- Van Campo, F., J. C. Duplessy, and M. Rossignol-Strick, Climatic conditions deduced from a 150 kyr oxygen isotope-pollen record from the Arabian Sea, *Nature*, **296**, 56-59, 1982.
- Webb, T., III, P. J. Bartlein, and J. E. Kutzbach, Climatic change in eastern North America during the past 18,000 years: Comparisons of pollen data with model results, in *The Geology of North America, vol. K-3, North America and Adjacent Oceans During the Last Deglaciation*, edited by W. F. Ruddiman and H. E. Wright, Jr., pp. 447-462, Geological Society of America, Boulder, Colo., 1987.
- Williams, J., R. G. Barry, and W. M. Washington, Simulation of the atmospheric circulation using the NCAR global circulation model with ice age boundary conditions, *J. Appl. Meteorol.*, **13**, 305-317, 1974.
- Wintle, A. G., N. J. Shackleton, and J. P. Lautridou, Thermoluminescence dating of periods of loess deposition and soil formation in Normandy, *Nature*, **310**, 491-493, 1984.

S. Joussaume, Laboratoire de Modélisation du Climat et de l'Environnement, Direction des Sciences de la Matière - Batiment 709, Centre d'Etudes de Saclay, 91191 Gif-sur-Yvette, France.

(Received June 4, 1991;  
revised July 24, 1992;  
accepted August 10, 1992.)